1 **Molecular chaperone ability to inhibit amyloid-derived neurotoxicity, but not**

2 **amorphous protein aggregation, depends on a conserved pH-sensitive Asp residue**

3

4 Gefei Chen[1*], Yuniesky Andrade-Talavera[2#], Xueying Zhong[3#], Sameer Hassan[1#], Henrik

5 Biverstal[1,4], Helen Poska[1,5], Axel Abelein[1], Axel Leppert[1], Nina Kronqvist[1], Anna Rising[1],

6 Hans Hebert[3], Philip J.B. Koeck[3], André Fisahn[2], Jan Johansson[1]

7

8 [1]Department of Biosciences and Nutrition, Karolinska Institutet, 141 52 Huddinge, Sweden

9 [2]Department of Neurobiology, Care Sciences and Society, Center for Alzheimer Research,

10 Division of Neurogeriatrics, Neuronal Oscillations Laboratory, Karolinska Institutet, 171 77

11 Stockholm, Sweden

12 [3]School of Engineering Sciences in Chemistry, Biotechnology and Health, Department of

13 Biomedical Engineering and Health Systems, KTH Royal Institute of Technology, 141 52

14 Huddinge, Sweden

15 [4]Department of Physical Organic Chemistry, Latvian Institute of Organic Synthesis, Riga

16 LV-1006, Latvia

17 [5]School of Natural Sciences and Health, Tallinn University, Tallinn, Estonia

18 # These authors contributed equally.

19 *Corresponding author, E-mail: gefei.chen@ki.se

20

21

22

23

24

25

26

27

28

29

30

31

32

33

34

Abstract

Proteins can self-assemble into amyloid fibrils or amorphous aggregates and thereby cause disease. Molecular chaperones can prevent both these types of protein aggregation, but the respective mechanisms are not fully understood. The BRICHOS domain constitutes a disease-associated small heat shock protein-like chaperone family, with activities against both amyloid toxicity and amorphous protein aggregation. Here, we show that the activity of two BRICHOS domain families against Alzheimer's disease associated amyloid-β neurotoxicity to mouse hippocampi *in vitro* depends on a conserved aspartate residue, while the ability to suppress amorphous protein aggregation is unchanged by Asp to Asn mutations. The conserved Asp in its ionized state promotes structural flexibility of the BRICHOS domain and has a pKa value between pH 6.0–7.0, suggesting that chaperone effects against amyloid toxicity can be affected by physiological pH variations. Finally, the Asp is evolutionarily highly conserved in >3000 analysed BRICHOS domains but is replaced by Asn in some BRICHOS families and animal species, indicating independent evolution of molecular chaperone activities against amyloid fibril formation and non-fibrillar amorphous protein aggregation.

Introduction

54 Proteins and peptides can self-assemble into highly ordered fibrillar structures as well as into

55 smaller oligomers with less well-defined structures but apparently stronger ability to cause

56 toxicity to cells. These phenomena are linked to so-called amyloid diseases, which

57 encompass about forty severe human diseases including interstitial lung disease (ILD) and

58 Alzheimer's disease (AD)(1, 2). A multitude of proteins have been shown to form amyloid

59 fibrils *in vitro* and generate cytotoxic species, yet they are not found in association with

60 disease, which suggest that efficient chaperoning and/or other defence systems are in place(3,

61 4). Molecular chaperones prevent protein aggregation and cytotoxicity(5), and

62 chaperonopathy might occur during *e.g.* ageing and by genetic mutations, leading to protein

63 misfolding disorders(6-8). However, no clear correlation between the clinical phenotype and

64 the severity of anti-aggregation defects of disease-causing molecular chaperone mutations

65 has been shown for *e.g.,* DNAJB6b and HSPB1(9, 10).

66

67 Many exceptionally amyloidogenic polypeptides are expressed as proproteins which are

68 subjected to proteolytic cleavage to release the amyloidogenic fragments(11-13). Some of

69 these proproteins contain the small heat shock protein (sHSP)-like domain BRICHOS,

70 initially found in integral membrane protein 2B (also called **Bri**2), **Cho**ndromodulin-1 and

71 prosurfactant protein C (pro**S**P-C)(14, 15). The BRICHOS domain is supposed to promote

72 the correct folding and prevent amyloid formation of the amyloid-prone region of its

73 proprotein during biosynthesis(16-18), and is released by proteolysis(19-21). Mutations in the

74 BRICHOS domain or in the proproteins are associated with different protein misfolding and

75 amyloid diseases(16, 22, 23), but the underlying pathogenic mechanisms are largely

76 unknown. The BRICHOS domain has been shown to have chaperone activities also in *trans*

77 against amyloid fibril formation and toxicity of several peptides associated with human

78 diseases(21, 24, 25) and has emerged as a model compound in studies of amyloid fibril

79 formation(26-29). AD relevant amyloid-β with 42 residues (Aβ42) forms amyloid fibrils via

80 several microscopic nucleation steps (*i.e.*, primary nucleation, elongation, and secondary

81 nucleation), whereby Aβ42 oligomers are generated, which are supposed to be the main toxic

82 species that drive AD development(27). The recombinant human (rh) BRICHOS domain

83 from proSP-C is an efficient inhibitor of amyloid toxicity of Aβ42 *in vitro* in mouse

84 hippocampal slice preparations, reducing the generation of toxic Aβ42 oligomers, but it is not

85 very competent to reduce the overall amyloid fibril formation rate(24, 27). *In vivo* proSP-C

86   BRICHOS has shown positive effects on locomotion and longevity when co-expressed with

87   Aβ42 in a *Drosophila* fruit fly model(30, 31). The rh Bri2 BRICHOS, on the other hand, is

88   efficient in inhibiting both Aβ42 amyloid fibril formation rate and toxicity by assembling into

89   differently sized species, of which monomers potently prevent neuronal network toxicity of

90   Aβ42, dimers strongly suppress Aβ fibril formation and large oligomers inhibit non-fibrillar

91   protein aggregation(24, 30, 32, 33). Interestingly, for the BRICHOS domains studied so far,

92   the ability to suppress amorphous protein aggregation, the canonical molecular chaperone

93   function, is not coupled to the ability to prevent amyloid fibril formation or toxicity. ProSP-C

94   BRICHOS essentially lacks activity against amorphous protein aggregation, while Bri2 and

95   Bri3 BRICHOS inhibit both fibrillar and non-fibrillar aggregation(32, 34). We could recently

96   explain the basis for this discrepancy by showing that the canonical chaperone activity to

97   suppress amorphous protein aggregation is determined by specific loop segments in

98   BRICHOS, while the activity against amyloid formation is independent of these segments

99   (Chen et al, submitted for publication).

100

101 Recently, a Bri2 BRICHOS mutant (R221E), designed to stabilize the monomeric

102 conformation, showed great potential in the prevention and treatment of AD by alleviating

103 Aβ42 neurotoxicity rather than its overall fibrillization rate(33). A corresponding mutation in

104 proSP-C BRICHOS (T187R) likewise generates monomers that bind to the smallest

105 emerging Aβ42 oligomers(28). Surprisingly, T187N mutation of human proSP-C BRICHOS

106 leads to ILD with amyloid deposits, while the T187R mutant is more efficient *in vitro* than

107 the wildtype against amyloid fibril formation(28, 35). Thus, understanding the molecular

108 mechanisms that regulate BRICHOS chaperone activities are of interest from a basic science

109 point of view and for the development of treatments against amyloid diseases. In the

110 BRICHOS superfamily, the secondary structure elements are highly conserved but the amino

111 acid sequence conservation is low, and only one aspartic acid residue (Asp, D) and two

112 cysteine residues that form a disulphide bridge were previously found to be strictly conserved,

113 from analyses of a rather small number of sequences(14, 33). The physiological function of

114 this Asp is unknown, yet two mutations of D105 in human proSP-C BRICHOS are linked to

115 ILD(16, 20, 36). Herein, we analysed all BRICHOS proproteins deposited in sequence

116 databases and studied experimentally how BRICHOS capacities against amyloid formation

117 and toxicity, as well as non-fibrillar protein aggregation is affected by the conserved Asp. We

118 found that the evolutionally conserved Asp is replaced by Asn in some BRICHOS families, is

119 protonated at physiological pH and is essential for preventing amyloid toxicity but not
120 amorphous aggregation.

121

122 **Results**

123 **Evolutionary analyses of BRICHOS domains**

124 As substantially more BRICHOS containing proteins have been described from genome
125 sequencing since the initial analyses were performed, we undertook detailed phylogenetic
126 and sequence analyses of all so far reported BRICHOS containing proteins. Amino acid
127 sequences of 3 355 BRICHOS precursors were extracted from the SMART database,
128 covering a broad distribution of 537 different metazoan species from worms to humans,
129 grouped into eleven phyla (**Fig. 1a and b**). After sorting out repetitive and incomplete
130 sequences, 2 019 BRICHOS sequences from 1 968 precursors were retained for further
131 analysis. These BRICHOS domains were separated into thirteen groups, which include
132 eleven previously known families (integral membrane protein 2A (ITM2A), ITM2B (also
133 called Bri2), ITM2C (also called Bri3), group I, gastrokine-1 (GKN1), GKN2, GKN3,
134 tenomodulin (TNMD), chondromodulin (CNMD, previously called LECTI), proSP-C,
135 BRICHOS containing domain 5 (BRICD5) and two novel families (group II and
136 antimicrobial peptide (AMP)) (**Fig. 1c centre and inner ring**, **supplementary Fig. 1**). The
137 BRICHOS domains in the AMP group were recently found in marine animals to help
138 antimicrobial peptides to fold correctly(37-39), while the BRICHOS domains in group II
139 have unknown functions.

140

141 Interestingly, analyses of the 1 968 precursors of the 2 019 BRICHOS domains showed that
142 there are a few BRICHOS containing proproteins that contain multiple BRICHOS domains
143 along with their corresponding amyloid-prone regions (**Fig. 1d and e, Supplementary Fig.**
144 **2**). Multiple BRICHOS domains were found in GKN1, proSP-C, CNMD and group II
145 families (**Fig. 1c outer ring**). In total 99% (1948 out of 1968) of BRICHOS precursors
146 contain a single BRICHOS domain, while 1% possess multiple BRICHOS domains (up to
147 nineteen BRICHOS domains were found in one precursor) (**Fig. 1f, Supplementary Fig. 2**).
148 The multiple BRICHOS domains within one precursor showed pairwise identities from 48%
149 to 97% (**Supplementary Table 1**), indicating that they arose by duplications. Alignment of
150 all compiled BRICHOS amino acid sequences showed that the Asp residue, which previously
151 was found to be strictly conserved, did not show 100% conservation in neither the single nor
152 the multiple BRICHOS domains (**Fig. 2a and b**, **Supplementary Fig. 3 and 4**). In the single

153   BRICHOS domains, 97% (1853 out of 1908) contain the conserved Asp, while 2.7% have

154   Asn, and the remaining 0.3% are distributed between Glu (E) and Ser (S) (**Fig. 2c**). Within

155   the multiple BRICHOS domains, the percentage having Asp was markedly decreased to 31%,

156   while instead 68% contain Asn, and one example with Glu was found (**Fig. 2d**). In the cases

157   of multiple BRICHOS containing proproteins, 85% have either Asp or Asn, and 15% utilize

158   both Asp and Asn (or Glu) (**Fig. 2e, Supplementary Fig. 2**). Among the BRICHOS domains

159   derived from single BRICHOS precursors, the ones having Asn were found in GKN1, GKN3,

160   ITM2A, and proSP-C BRICHOS families (**Fig. 2a and f**), and were mainly found in birds

161   (Aves, 81%) with only 19% from Mammalia (**Fig. 2f**). An interesting observation is that bird

162   surfactant lacks SP-C(40), so the BRICHOS containing proSP-C from birds likely have

163   evolved other functions than to generate SP-C. Surprisingly, all the non-Asp BRICHOS

164   domains from the multiple BRICHOS precursors were found in the GKN1 family and are all

165   from birds (**Fig. 2g**).

166

167   **Ionization and protonation of the Aspartate within a physiological pH range**

168   The results from the evolutionary studies prompted us to mutate the conserved Asp to Asn in

169   human BRICHOS domains from proSP-C (Asp105) and Bri2 (Asp148), which are the most

170   studied BRICHOS domains.

171

172   Size exclusion chromatography (SEC) showed that both wildtype and D105N rh proSP-C

173   BRICHOS adopt trimeric conformation, but the mutant formed more dimers and less

174   monomers than the wildtype protein (**Supplementary Fig. 5a**). Circular dichroism (CD)

175   spectroscopy showed rh proSP-C BRICHOS D105N is overall more structured than the

176   wildtype at neutral pH as judged from a shift from the minimum around 202 nm to around

177   207 nm, while at acidic pH the CD spectra are virtually identical (**Supplementary Fig. 5b**

178   **and c**). To see whether wildtype rh proSP-C BRICHOS titrates with an elevated pKa value

179   (compared to pKa of about 4.5 for free Asp in solution), we followed the CD signal at 204

180   nm of rh proSP-C BRICHOS between pH 7.0 and 5.0, which gave an apparent pKa value of

181   the transition of about 6.1 (**Fig. 2h, Supplementary Fig. 5b**). Notably, the CD spectra of rh

182   proSP-C BRICHOS D105N did not shift substantially between pH 5.5 and 8.0 (**Fig. 2h,**

183   **Supplementary Fig. 5c**), suggesting that protonation of D105 is a main determinant of the

184   observed conformational shift, and it may be the sole titrating residue in this pH range. To

185   confirm the pH-dependent conformational changes, we ran NMR spectroscopy on wildtype

186   rh proSP-C BRICHOS labelled with ^{15}N, ^{13}C and ^{2}H at different pHs. The comparison of the

6

187   ^{15}N-HSQC spectra at pH 5.5 and 7.2 showed clear chemical shift changes, supporting that rh

188   proSP-C BRICHOS undergoes structural changes in this pH range (**Supplementary Fig. 5d**).

189

190   Rh wildtype NT*-Bri2 BRICHOS(33) and rh NT*-Bri2 BRICHOS D148N showed similar

191   elution profiles on SEC (**Supplementary Fig. 5e**). After removal of the NT* solubility tag, rh

192   Bri2 BRICHOS D148N formed similar disulphide-dependent assembly states as the wildtype

193   protein (**Supplementary Fig. 5f–h**). However, the rh Bri2 BRICHOS D148N dimers are

194   exclusively disulphide-linked (**Supplementary Fig. 5h**, **Figure 5-figure supplement 5-**

195   **source data**), while the wildtype dimers are a mixture of disulphide-linked and non-covalent

196   species(32). Moreover, rh Bri2 BRICHOS D148N generated from the rh NT*-Bri2

197   BRICHOS D148N monomer fraction did not elute on SEC as a monomer but as a dimer,

198   while both the corresponding oligomers and dimers shared similar elution profiles as the

199   corresponding wildtype states (**Supplementary Fig. 5f and g**). This indicates that the rh Bri2

200   BRICHOS D148N monomers are not stable but form non-covalent dimers. Rh Bri2

201   BRICHOS D148N oligomers and dimers shared identical CD spectra as the corresponding

202   wildtype species, whereas the initially monomeric rh Bri2 BRICHOS D148N showed a

203   somewhat different CD spectrum compared to the wildtype monomers (**Supplementary Fig.**

204   **5i–l**), but which can be superimposed on the wildtype dimer spectrum (**Supplementary Fig.**

205   **5l**). This suggests the rh Bri2 BRICHOS D148N monomer mainly assembles into a dimer at

206   the concentration used for CD spectroscopy. As analysed by SEC, at one μmol L^{-1}, rh

207   wildtype Bri2 BRICHOS monomer migrated solely as a monomer, and with increasing

208   concentration, dimers were progressively formed (**Supplementary Fig. 6a, Supplementary**

209   **Fig. 7**). However, an equilibrium between dimers and monomers were seen even at 200 μmol

210   L^{-1} (**Supplementary Fig. 6a, Supplementary Fig. 7e**). In contrast, already at low

211   concentrations (0.5 μmol L^{-1}) rh Bri2 BRICHOS D148N showed an equilibrium between

212   dimers and monomers, approximately at a ratio of 1:1 (**Supplementary Fig. 6b,**

213   **Supplementary Fig. 8a**). With progressively increased concentrations rh Bri2 BRICHOS

214   D148N monomers transformed to dimers and at 100 μmol L^{-1} all proteins migrated as dimers

215   (**Supplementary Fig. 6b, Supplementary Fig. 8f**). To get further details on how rh Bri2

216   BRICHOS undergoes monomer-dimer transition, we analysed SEC profiles at different pHs.

217   At pH 7.0 to 8.0 both rh Bri2 BRICHOS D148N and wildtype monomers showed similar

218   elution volumes (**Supplementary Fig. 6c and d**). However, at pH 6.0 rh wildtype Bri2

219   BRICHOS elutes as a dimer, whereas the D148N mutant did not show any significant

220   difference compared to the elution volume at pH 7.0 and 8.0 (**Supplementary Fig. 6c and d**).

221   This suggests that at pH between 7.0 and 6.0 Asp148 can be protonated with subsequent shift

222   of the dimer-monomer equilibrium towards dimers. To corroborate the supposition that

223   Asp148 titrates between pH 6.0 and 7.0 we turned to a rh Bri2 BRICHOS variant with

224   Thr206 replaced by Trp (T206W) that displayed an identical oligomerization profile as the rh

225   wildtype Bri2 BRICHOS (**Supplementary Fig. 9a**), but a different Trp fluorescence profile

226   in the monomeric state compared to the dimeric state (**Supplementary Fig. 9b**). In

227   agreement with SEC data, titration of the rh Bri2 BRICHOS Trp mutant showed a

228   fluorescence evolution (monomer/dimer transition) with a pKa of 6.7 (**Fig. 2i,**

229   **Supplementary Fig. 9c**).

230

231   These observations indicate that the D148N mutation in rh Bri2 BRICHOS promotes

232   monomer to dimer conversion, and mimics pH-induced dimerization of the wildtype

233   monomers with an apparent pKa of 6.7, but it does not significantly change the assembly of

234   dimers into larger oligomers. Analogously, the mutation D105N in rh proSP-C BRICHOS

235   results in a more compact conformation and possibly more complete assembly into trimers,

236   and the wildtype rh proSP-C BRICHOS conformational shift by CD titrates with an apparent

237   pKa of 6.1.

238

239   **The conserved Asp of BRICHOS is essential for the capacity to prevent Aβ42-induced**

240   **neurotoxicity**

241   To investigate the importance for the ability to alleviate amyloid-induced neurotoxicity, we

242   tested the efficacies of Asp to Asn mutated vs. wildtype BRICHOS in preventing Aβ42-

243   induced reduction of γ oscillations in mouse hippocampal slices. γ oscillations correlate with

244   learning, memory, cognition and other higher processes in the brain[41, 42] and progressive

245   cognitive decline observed in AD goes hand-in-hand with a progressive decrease of γ

246   oscillations[43-45]. The BRICHOS domains from human proSP-C and Bri2 can efficiently

247   prevent Aβ42-induced decline in hippocampal γ oscillations[27, 30, 32, 33, 46]. In addition,

248   rh Bri2 BRICHOS rescues γ oscillations and neuronal network dynamics from Aβ42-induced

249   impairment at hippocampal CA3 area *ex vivo*[47]. We recorded γ oscillations in hippocampal

250   slices from wildtype C57BL/6 mice preincubated for 15 min either with 50 nmol L^{-1} Aβ42

251   alone, or co-incubated with 100 nmol L^{-1} rh wildtype or D105N proSP-C BRICHOS (**Fig.**

252   **3a**). γ oscillations were elicited by application of 100 nmol L^{-1} kainic acid (KA) and allowed

253   to stabilize for 30 min prior to any recordings. As previously observed[27, 30, 46], 100 nmol

254   L^{-1} wildtype proSP-C BRICHOS prevented Aβ42-induced degradation of γ oscillations,

255   which were remained at control levels (**Fig. 3b and c**, control: $1.7 \pm 0.16 \times 10^{-8}$ V^2 Hz^{-1}, n=

256   20; Aβ42: $0.34 \pm 0.06 \times 10^{-8}$ V^2 Hz^{-1}, n= 14, *p*< 0.0001 vs. control; + rh wildtype proSP-C

257   BRICHOS: $1.41 \pm 0.24 \times 10^{-8}$ V^2 Hz^{-1}, n= 9) (**Supplementary Table 2**, **Figure 3-source**

258   **data**). By contrast, rh proSP-C BRICHOS D105N showed a complete loss of the preventative

259   efficacy at the same concentration (**Fig. 3b and c**, rh proSP-C BRICHOS D105N: $0.36 \pm$

260   0.09×10^{-08} V^2 Hz^{-1}, n= 9, *p*= 0.0202 vs. rh wildtype proSP-C BRICHOS, *p*= 0.0002 vs.

261   control, *p*> 0.9999 vs. Aβ42) (**Supplementary Table 2**, **Figure 3-source data**). We have

262   previously observed that the rh Bri2 BRICHOS monomer is most efficient at preventing

263   Aβ42 induced degradation of γ oscillations(32, 33). We therefore tested whether the D148N

264   mutation could affect the efficacy of rh Bri2 BRICHOS monomers. Rh Bri2 BRICHOS

265   D148N monomers (50 nmol L^{-1}) showed reduced tendency of potency to prevent Aβ42-

266   induced neurotoxicity compared to wildtype monomers (50 nmol L^{-1}), but did not completely

267   lose preventative efficacy, as observed for rh proSP-C BRICHOS D105N (**Fig. 3d and e**, rh

268   wildtype Bri2 BRICHOS monomers: $1.35 \pm 0.29 \times 10^{-8}$ V^2 Hz^{-1}, n= 8, *p*> 0.9999 vs. control;

269   rh Bri2-BRICHOS D148N monomers: $0.7 \pm 0.14 \times 10^{-8}$ V^2 Hz^{-1}, n= 11, *p*= 0.3494 vs. rh

270   wildtype Bri2 BRICHOS monomers, *p*= 0.003 vs. control, *p*= 0.6991 vs. Aβ42)

271   (**Supplementary Table 2**, **Figure 3-source data**). These results suggest that the

272   phylogenetically conserved Aspartate plays a crucial role in maintaining the anti-amyloid

273   neurotoxicity capacity of BRICHOS.

274

275   **The conserved Asp of BRICHOS is not important for canonical chaperone activity**

276   **against amorphous protein aggregation or Bri2 BRICHOS oligomer structure**

277   The rh wildtype Bri2 BRICHOS oligomers are efficient molecular chaperones against non-

278   fibrillar protein aggregation, evaluated by thermo-induced citrate synthase aggregation as a

279   model(32). This was found to be true also for the rh Bri2 BRICHOS D148N oligomers (**Fig.**

280   **5a** and **b**). Similarly, the D105N mutation did not show any effects on the capacity of rh

281   proSP-C BRICHOS trimer against amorphous protein aggregation, *i.e.*, both the wildtype and

282   D105N mutant are essentially inactive as regards canonical chaperone activity

283   (**Supplementary Fig. 10a**). This shows a strong difference in the importance of the

284   conserved Asp in BRICHOS for activity against amyloid toxicity compared to activity

285   against amorphous protein aggregation.

286

287 Although the D148N mutation changed the balance between monomers and dimers of rh Bri2

288 BRICHOS, the mutant still formed large oligomeric species with a similar secondary

289 structure as wildtype oligomers (**Supplementary Fig. 5e, g and i**). We isolated rh Bri2

290 BRICHOS D148N oligomers by SEC, recorded transmission electron microscopy (TEM)

291 micrographs and calculated 3D reconstructions (**Fig. 4c and d, Supplementary Fig. 10b and**

292 **c**, **Figure 4-source data**). The micrographs and 2D class averages revealed mostly

293 homogenous large assemblies with two-fold symmetry (**Fig. 4c**). As a result, an EM map was

294 reconstructed with D2 symmetry from 10 223 manually extracted single particles (**Fig. 4d**,

295 **Figure 4-source data**). The rh Bri2 BRICHOS D148N oligomer 3D model and the one from

296 the wildtype oligomers(32) overlap and share overall similar shape and volume (**Fig. 4e**,

297 **Figure 4-source data**), suggesting that the overall structure of the large Bri2 BRICHOS

298 oligomers is not noticeably changed when Asp148 is mutated to Asn.

299

300 **Molecular mechanisms underlying the importance of the conserved Asp of BRICHOS**

301 **for**

302 **ability to suppress Aβ42 neurotoxicity**

303 To further explore whether the diminished BRICHOS capacity against amyloid neurotoxicity

304 caused by Asp to Asn mutation correlates with the activity of suppressing macroscopic

305 amyloid fibril formation, we used thioflavin T (ThT)(48) fluorescence to monitor the kinetics

306 of Aβ42 fibril formation in the absence and presence of different concentrations of rh Bri2 or

307 proSP-C BRICHOS (**Fig. 5**). Both the rh wildtype proSP-C BRICHOS and the D105N

308 mutant showed dose-dependent progressive reduction of Aβ42 fibril formation at

309 substoichiometric concentrations, and the aggregation kinetics follows a typical sigmoidal

310 behavior (**Fig. 5a and d–f, Supplementary Fig. 11a-c**). The Aβ42 fibrillization half time,

311 $\tau_{1/2}$, increases with increasing rh proSP-C BRICHOS concentration (**Fig. 5b**), while the

312 maximum rate of Aβ42 aggregation, r_{max}, shows a mono-exponential decline (**Fig. 5c**).

313 Interestingly, rh proSP-C BRICHOS D105N showed remarkably improved inhibition on

314 Aβ42 fibril formation compared to the wildtype, manifested with both $\tau_{1/2}$ and r_{max} (**Fig. 5a–**

315 **c**), which is opposite compared to the effects on the capacity to prevent Aβ42-induced

316 neurotoxicity (**Fig. 3**). On the other hand, similarly, the rh wildtype Bri2 BRICHOS

317 monomers showed similar effects on $\tau_{1/2}$ and r_{max} of Aβ42 fibrillization as reported (**Fig. 5g–**

318 **i**)(32). The rh Bri2 BRICHOS D148N oligomers, dimers and monomers also presented dose-

319 dependent inhibition on Aβ42 fibril formation with typical sigmoidal behavior (**Fig. 5g–i,**

320   **Supplementary Fig. 12**). Along the same lines, compared to wildtype monomers, the D148N

321   monomers were significantly more efficient in inhibiting Aβ42 fibril formation (**Fig. 5g–i**),

322   suggesting the Asp to Asn mutation pronouncedly enhances BRICHOS activity against

323   overall fibril formation. The D148N monomers and dimers showed very similar inhibitory

324   effects on Aβ42 fibrillization (**Supplementary Fig. 12a and b**), which likely can be

325   explained by that D148N monomers and dimers are in equilibrium (**Supplementary Fig. 6b**

326   **and 8**).

327

328   To find out the molecular mechanisms underlying how the Asp to Asn mutation decreases

329   BRICHOS capacity against Aβ42 neurotoxicity but enhances its inhibitory activity against

330   overall Aβ42 fibril formation, we investigated the effects of both rh wildtype BRICHOS and

331   the corresponding Asp to Asn mutants on Aβ42 amyloid fibril formation and related

332   microscopic events. Aβ42 fibrillization kinetics are described by a set of microscopic rate

333   constants, *i.e.*, primary (k_n) and surface-catalyzed secondary nucleation (k_2) as well as

334   elongation (k_+)(49), and perturbations of the individual microscopic rates are most relevant

335   since their relative contributions determine the generation of nucleation units, which might be

336   linked to the neurotoxic Aβ42 oligomeric species(27, 50). To evaluate the effects on

337   individual microscopic processes, we performed global fits of the kinetics data sets at

338   constant Aβ42 and different BRICHOS concentrations for both rh wildtype proSP-C and the

339   D105N mutant, where the fits were constrained such that only one single rate constant, *i.e., k_n,*

340   k_2 or k_+, is the sole fitting parameter (**Fig. 5d-f, Supplementary Fig. 11a–c**). As previously

341   described(27), the rh wildtype proSP-C BRICHOS mainly interfered with the secondary

342   nucleation, indicated by the perfect fits when k_2 was the sole global fitting rate constant

343   (**Supplementary Fig. 11a–c**). Also, the secondary nucleation rate k_2 as the sole fitting

344   parameter gave the best fits for the Aβ42 fibrillization kinetics with rh proSP-C BRICHOS

345   D105N (**Fig. 5d-e**), but with worse quality compared to the wildtype, especially for the start

346   of the aggregation traces. This suggests that a complex microscopic mechanism is present,

347   which might also include fibril-end elongation (k_+) and/or primary nucleation (k_n) in addition

348   to secondary nucleation (k_2). To further study whether the fibril-end elongation process or the

349   primary nucleation are affected in the presence of rh proSP-C BRICHOS D105N and

350   wildtype forms, we determined aggregation kinetics in the presence of a high initial fibril

351   seed concentration(49) and surface plasmon resonance (SPR) analysis. With seeding, the

352   fibrillization traces typically follow a concave aggregation behavior (**Supplementary Fig.**

11

353   **11d and e**), where the initial slope is directly proportional to the elongation rate k_+. These

354   seeding experiments revealed that rh proSP-C BRICHOS D105N decreases the elongation in

355   a dose-dependent manner, and already at low concentrations fibril-end elongation is

356   noticeably retarded (**Fig. 5j, Supplementary Fig. 11e**). The rh wildtype proSP-C BRICHOS,

357   in contrast, showed only slight effects on fibril-end elongation (**Fig. 5j, Supplementary Fig.**

358   **11d**), which is further supported by immuno-transmission electron microscopy (immuno-EM)

359   images where both rh proSP-C BRICHOS D105N and the wildtype attach along the Aβ42

360   fibril surface, however, the fibril ends are apparently mainly blocked by the D105N mutant

361   (**Fig. 5k**). Additionally, SPR analyses of Aβ42 monomers immobilized on a sensor chip

362   indicated that rh wildtype proSP-C BRICHOS showed weak binding to the immobilized

363   Aβ42 monomers in line with previous reports(27, 28). The D105N mutation significantly

364   enhanced the BRICHOS-Aβ42 monomer interactions (**Supplementary Fig. 11f**) with an

365   apparent affinity value K_D around 5 μmol L^{-1} (**Fig. 5l**) from global kinetics fits, and under

366   steady-state conditions a K_D value of around 25 μmol L^{-1} was obtained (**Supplementary Fig.**

367   **11g**). Interfering with primary nucleation (k_n) delays Aβ42 fibril formation without changing

368   the total number of oligomers generated, suppressing the secondary nucleation (k_2) efficiently

369   prevents the generation of oligomers, while blocking elongation (k_+) significantly increases

370   the number of oligomers formed(27). Of relevance for the results on Aβ42 neurotoxicity of

371   wildtype vs D105N proSP-C BRICHOS (**Fig. 3**), we found that in the presence of equimolar

372   ratio of rh proSP-C BRICHOS D105N, the Aβ42 fibrillization reaction generated

373   approximately 5.2 times more oligomers than from Aβ42 alone, by significantly suppressing

374   the fibril end elongation process, while the wildtype only showed slight effects (**Fig. 5j**

375   **insets**). These observations show that both rh proSP-C BRICHOS D105N and the wildtype

376   protein reduce Aβ42 fibrillization by blocking the surface-catalyzed secondary nucleation,

377   while fibril-end elongation and possibility primary nucleation are substantially affected only

378   by the D105N mutant. These results offer a molecular explanation to the observed loss of

379   inhibitory effects of the rh proSP-C BRICHOS mutant on neurotoxic Aβ42 oligomer

380   generation.

381

382   To further study the mechanism underlying the reshaped interference of BRICHOS with

383   Aβ42 monomer and fibrils, we used the non-polar fluorescent dye bis-ANS to probe the

384   exposure of hydrophobic areas. Bis-ANS shows a blue shift of the emission maximum and

385   increased emission intensity upon binding to exposed hydrophobic protein surfaces, which

386 has been applied to rh wildtype Bri2 and proSP-C BRICHOS(32, 51, 52). When incubated

387 with bis-ANS, rh wildtype proSP-C BRICHOS gave an increase of emission intensity

388 compared to bis-ANS in buffer, and a blue shift of the emission maximum from about 520

389 nm to 495 nm (**Supplementary Fig. 11h**). Notably, the blue shift and the intensity increase

390 for the D105N mutant at pH 8.0 are more pronounced compared to the wildtype protein

391 (**Supplementary Fig. 11h**), showing that D105N results in more exposed hydrophobic areas,

392 which may be important for Aβ42 fibril-end binding(32, 33) and monomer binding.

393 Interestingly, when incubating bisANS with rh wildtype proSP-C BRICHOS at pH 6.0 an

394 identical fluorescence spectrum as for the D105N mutant at pH 8.0 was observed

395 (**Supplementary Fig. 11h**), indicating that the D105N mutation gives similar effects as

396 protonating Asp105. For Bri2 BRICHOS, dimers were found previously to be most efficient

397 in preventing Aβ42 overall fibril formation compared to the monomers and oligomers, while

398 the monomers are most potent in preventing Aβ42 induced disruption of neuronal network

399 activity(32, 33). The microscopic mechanisms of rh Bri2 BRICHOS D148N species were

400 similar to the wildtype species, both the secondary nucleation and elongation of Aβ42 were

401 affected (**Supplementary Fig. 12c–k**). However, the equilibrium between monomer and

402 dimer was modified by the Asp to Asn mutant towards the dimer (**Supplementary Fig. 6a**

403 **and b, Supplementary Fig. 7 and 8**), thus reducing the monomer that is predominantly

404 active against Aβ42-induced neurotoxicity but increasing the dimer fraction, which is most

405 active against Aβ42 fibril formation.

406

407 **Discussion**

408 In this work, we show that the capacity of sHSP-like chaperone domain BRICHOS to inhibit

409 amyloid-associated neurotoxicity is dependent on a phylogenetically conserved Asp, whereas

410 the capacity to suppress non-fibrillar, amorphous protein aggregation is not affected by

411 mutating this Asp to Asn. Moreover, conformational changes occur as a result of Asp to Asn

412 mutations in both proSP-C and Bri2 BRICHOS, those changes can partly be mimicked by

413 lowered pH and the conserved Asp titrates with an apparent pKa of about 6.5 in both

414 BRICHOS domains studied.

415

416 The Asp residue studied herein is the only conserved non-Cys residue in all known

417 BRICHOS domains and two mutations of this residue in human proSP-C BRICHOS (D105)

418 are linked to ILD(16, 20, 36). Based on molecular dynamic simulation(16), monomeric

13

419   wildtype proSP-C BRICHOS and the D105N mutant behaved differently: only minor
420   conformational changes were seen in the mutant, but several large-scale changes occurred in
421   the wildtype at moderately elevated temperatures, which resulted in a more loosely folded
422   structure. We can rationalize our results against this background (**Fig. 6a and b**). D105N
423   mutation in rh proSP-C BRICHOS indeed results in a more ordered conformation and
424   apparently more efficient trimer formation, while D148N mutation of rh Bri2 BRICHOS
425   results in more readily transition of monomers to more compact dimers (**Supplementary Fig.**
426   **5a and f**). Similar effects as observed in the mutants were seen for the wildtype proteins
427   when pH was lowered to 6-7 (**Fig. 2h and i**). This suggests that a negatively charged Asp
428   side-chain is necessary for maintaining a "loose" flexible state of the BRICHOS subunit and
429   that protonation, or replacement with a neutral Asn, results in a more "compact" state that is
430   prone to form oligomers. In the open conformation, BRICHOS is efficient in alleviating
431   Aβ42 amyloid neurotoxicity, while the compact conformation is more potent against overall
432   amyloid fibril formation but inefficient against amyloid induced neurotoxicity (**Fig. 6b**).
433   Interestingly, in brains of AD patients the pH is lower than that in the brains of healthy
434   individuals(53), and at low pH Aβ can form fibrils more efficiently than at neutral pH(54).

435

436   The crystal structure of rh proSP-C BRICHOS, the only available high-resolution structure of
437   a BRICHOS domain, gives limited information about the local environment of the conserved
438   Asp since electron density is lacking for the part N-terminally of the juxtaposed helix 2(16).
439   However, an inspection of amino acid sequence alignments of BRICHOS domains from all
440   families show that there is a well conserved carboxylate residue situated just upstream of
441   helix 2 (**Supplementary Fig. 3**, positions 176-180), and its location close to the sidechain of
442   the strictly conserved Asp may contribute to the apparently elevated pKa values of D105 and
443   D148 now observed. The distant evolutionary relationship between Bri2 and proSP-C
444   BRICHOS domains, with <20% sequence identities, makes it likely that the common effects
445   now observed between them also apply to other BRICHOS domains that exhibit similar
446   evolutionary distances. Therefore, an elevated pKa value of the only strictly conserved non-
447   Cys residue, as now found for proSP-C and Bri2 BRICHOS, is probably relevant for a
448   common function of all BRICHOS domains, which thus likely requires a maintained "loose"
449   conformation. Our results indicate that such a hypothetical common function is likely to be
450   related to prevention of amyloid toxicity rather than prevention of amorphous protein
451   aggregation. So far, molecular chaperones or chaperone-like domains have not been much
452   studied extensively as regards sensitivity to pH. One exception is clusterin, whose activity is

453 enhanced at mildly acidic pH, which appears to result from an increase in regions with
454 solvent-exposed hydrophobicity, but independent of any major changes in secondary or
455 tertiary structure(55). The phylogenetic analyses showed the presence of the BRICHOS
456 domain in a broad array of proproteins and species. In some cases where multiple BRICHOS
457 domains are found, the conserved Asp is preferentially replaced with Asn (**Fig. 1 and 2**).
458 Considering the experimental results herein this may suggest that BRICHOS has adopted
459 different types of molecular chaperone activities during evolution.

460

461 Molecule chaperones are essential guards of all living cells, while the chaperoning
462 abnormality may cause disease—chaperonopathy. The chaperoning capacities of BRICHOS
463 domain against amyloid neurotoxicity and fibril formation can apparently be modulated by a
464 conserved Asp in response to pH changes. In the human brain, pH decreases with aging(56),
465 and also pH is significantly lower in patients than in heathy controls in different human brain
466 disorders(53, 57). The observed phenomenon in this study suggests the possibility that
467 microenvironmental changes may lead to human disease. The results here are based on *in*
468 *vitro* and *ex vivo* experiments, and further *in vivo* work that focuses on the activities of
469 BRICHOS and pH-mediated regulation can shed further light on this.

470

471 **Materials and Methods**

472 **Phylogenetic analysis of BRICHOS domain**

473 From the SMART database(58), 3 355 BRICHOS sequences were downloaded while the sole
474 bacterial BRICHOS precursor (*Paeniclostridium sordellii* ATCC 9714) was not included.
475 Incomplete sequences were filtered out, resulting in total of 3 190 sequences. Identical
476 sequences were filtered by means of CD-HIT(59), with a threshold of 100% of sequence
477 identity, which gave 3 093 amino acid sequences. The hidden markov model profile (HMM)
478 of BRICHOS (PF04089) was extracted from PFAM database(60). The CD-HIT filtered
479 BRICHOS protein sequences were then scanned against the HMM profile using HMMER
480 software v3.3.2(61) with an E-value cut-off less than 1.0×10^{-5}. An in-house python script was
481 written to filter out the significant BRICHOS proteins from the HMM result file and to
482 extract the BRICHOS domain sequences (each BRICHOS amino acid sequence was extended
483 six residues upstream from the BRICHOS domain starting position defined by PFAM).
484 Further, BRICHOS domain sequences less than 68 aa were removed as one rodent BRICHOS
485 domain is just 69 residues and still functional against amyloid fibril formation(62), which
486 eventually generated 2 019 BRICHOS sequences. The multiple sequence alignment of the 2

15

487   019 BRICHOS domain sequences were created using MAFFT alignment server with the

488   default settings(63), and the sequence logo was generated using Weblogo webserver(64).

489   RAxML HPC(v8.2.10)(65) was employed for constructing the phylogenetic tree using the

490   PROTGAMMAAUTO model with 100 times bootstrap iterations. The tree shown in this

491   study was visualized using the Interactive Tree of Life (iTOL) server(66) and Geneious

492   software. The taxonomy tree common for species that contain BRICHOS precursors were

493   generated   by   NCBI   Taxonomy

494   (https://www.ncbi.nlm.nih.gov/Taxonomy/CommonTree/wwwcmt.cgi) and visualized by

495   Geneious software.

496

497   **Rh Bri2 BRICHOS and rh proSP-C BRICHOS wildtype and mutant preparation**

498   For   generating   rh   Bri2   BRICHOS   D148N,   the   amplification   primers   5'-

499   ATAGTGATCCTGCCAACATTGATAACTTTAACAAGAAACTTACA-3'   and   5'-

500   TGTAAGTTTCTTGTTAAAGTTATGAACAATGTTGGCAGGATCACTAT-3'   were

501   synthesized. With the wildtype NT*-Bri2 BRICHOS (corresponding to the solubility tag NT*

502   followed by Bri2 residues 113–231(32, 67)) plasmid as PCR template Bri2 BRICHOS

503   D148N was obtained with QuikChange II XL Site-Directed Mutagenesis Kit (Agilent, US),

504   and the DNA sequence was confirmed (GATC Bioteq, Germany). Similarly, the amino acid

505   Thr at position 206 was mutated to Trp using KAPA HiFi HotStart ReadyMix PCR Kit (Kapa

506   Biosystems,   USA)   together   with   the   designed   complementary   primers   (5'-

507   CCTATCTGATTCATGAGCACATGGTTATTTGGGATCGCATTGAAAAC-3'   and   5'-

508   GTTTTCAATGCGATCCCAAATAACCATGTGCTCATGAATCAGATAGG-3')   and

509   verified by sequencing (Eurofins Genomics). As described(32, 33) , the Bri2 BRICHOS

510   variants were expressed in SHuffle T7 *E. coli* cells. Briefly, the cells were incubated at 30°C

511   in LB medium with 15 μg mL^{-1} kanamycin until an OD$_{600\ nm}$ around 0.9. For overnight

512   expression, the temperature was lowered to 20°C, and 0.5 mmol L^{-1} (final concentration)

513   isopropyl β-D-1-thiogalactopyranoside (IPTG) was added. The induced cells were harvested

514   by centrifugation (4°C, 7 000 ×g) and the cell pellets were resuspended in 20 mmol L^{-1} Tris

515   pH 8.0. After 5 min sonication (2 s on, 2 s off, 65% power) on ice, the lysate was centrifuged

516   (4°C, 24 000 ×g) for 30 min and the protein of interest was isolated with a Ni-NTA column.

517   To remove the His$_6$-NT* part, the target proteins were cleaved with thrombin (1:1 000, w/w)

518   at 4°C overnight and loaded over a second Ni-NTA column. Different species of rh Bri2

519   BRICHOS variants were isolated and analysed by Superdex 200 PG, 200 GL or 75 PG

16

520 columns (GE Healthcare, UK) using an ÄKTA system (GE Healthcare, UK) with buffer of

521 20 mmol L^{-1} NaPi (Sodium Phosphate) with 0.2 mmol L^{-1} EDTA at different pHs. For

522 generating rh proSP-C BRICHOS D105N, the PCR primers 5'-

523 CACTGGCCTCGTGGTGTATAACTACCAGCAGCTGCTGATCGC-3' and 5'-

524 GCGATCAGCAGCTGCTGGTAGTTATACACCACGAGGCCAGTG -3' were synthesized.

525 With the wildtype proSP-C BRICHOS (corresponding to the solubility tag thioredoxin

526 followed by proSP-C residues 86–197(16)) plasmid as PCR template, proSP-C BRICHOS

527 D105N was obtained with QuikChange II XL Site-Directed Mutagenesis Kit (Agilent, US),

528 and the DNA sequence was confirmed (GATC Bioteq, Germany). The expression and

529 purification were performed as described(16, 68). Briefly, both wildtype proSP-C BRICHOS

530 and the D105N mutant were expressed in Origami 2 (DE3) pLysS *E. coli* cells. The cells

531 were grown at 37°C in LB medium containing 100 μg mL^{-1} ampicillin until an $OD_{600\ nm}$

532 around 0.9. The temperature was lowered to 25°C and 0.5 mmol L^{-1} (final concentration)

533 IPTG was added for overnight expression. The cells were harvested by centrifugation at 7

534 000 × *g* for 20 min, and the cell pellets were resuspended in 20 mmol L^{-1} Tris pH 8.0. The

535 protein was purified using Ni-NTA column and ion exchange chromatography (QFF, GE

536 Healthcare). Thrombin (1:1 000, w/w) was used to remove the thioredoxin tag. The purified

537 rh proSP-C BRICHOS variants were analysed by Superdex 200 GL columns (GE Healthcare,

538 UK) using an ÄKTA system (GE Healthcare, UK). The BRICHOS mutants in this study

539 were expressed and purified in parallel with their wildtype counterparts.

540

541 **NMR spectroscopy**

542 For the NMR experiments, gene fragment encoding human proSP-C BRICHOS was

543 transformed into SHuffle T7 *E. coli* cells and was grown in LB with gradually increasing

544 D_2O content (25%, 50%,75% and 100%). At 100% D_2O, 1 mL LB was used to inoculate 100

545 mL M9 in 100% D_2O enriched with ^{15}N H_4Cl and ^{13}C glucose, and was grown over night at

546 31°C. After overnight incubation, the 100 mL was added to 900 mL M9 in D_2O enriched

547 with ^{15}N and ^{13}C and grown at 30°C until $OD_{600\ nm}$ was around 0.8. The temperature was

548 lowered to 20°C and 0.5 mmol L^{-1} (final concentration) IPTG was added for overnight

549 expression. The purification was performed as described above.

550

551 2D ^1H-^{15}N TROSY-HSQC experiments were obtained at 37°C on Bruker 800 MHz

552 spectrometer equipped with a TCI cryogenic probe. Spectra were processed with the software

553 NMRPipe and visualized using Sparky NMR. The concentrations of ^2H, ^{15}N,^{13}C-labeled

17

554   proSP-C was 288 µmol L^{-1} in 20 mmol L^{-1} ammonium acetate pH 7.2 and 229 µmol L^{-1} in 20

555   mmol L^{-1} ammonium acetate pH 5.5, both in 90% H$_2$O/10% D$_2$O.

556

557   **Circular dichroism and fluorescence spectroscopy and aggregation analyses**

558   CD spectra were recorded in 1 mm path length quartz cuvettes at 25°C from 260 to 185 nm in

559   a J-1500 Circular Dichroism Spectrophotometer (JASCO, Japan) with a protein concentration

560   of 4.2–10 µmol L^{-1}. The bandwidth was set to 1 nm, data pitch 0.5 nm, and scanning speed

561   50 nm min^{-1}. The spectra shown are averages of five consecutive scans.

562

563   Citrate synthase from porcine heart (Sigma-Aldrich, Germany) was diluted in 40 mmol L^{-1}

564   HEPES/KOH pH 7.5 to 600 nmol L^{-1} (calculated from a molecular weight of 85 kDa

565   corresponding to a dimer(69)) and then equilibrated at 45°C with and without different

566   concentrations of rh Bri2 BRICHOS D148N oligomer or proSP-C BRICHOS variants. The

567   aggregation kinetics were measured by reading the apparent increase in absorbance at 360 nm

568   under quiescent conditions using a microplate reader (FLUOStar Galaxy from BMG Labtech,

569   Offenberg, Germany).

570

571   One µmol L^{-1}, calculated for the monomeric subunit, of different rh BRICHOS in 20 mmol L^{-1}

572   NaPi pH 8.0 or pH 6.0 were incubated at 25°C with 2 µmol L^{-1} bis-ANS (4,4'-

573   Bis(phenylamino)-[1,1'-binaphthalene]-5,5'-disulfonic acid dipotassium salt) for 10 min, and

574   the fluorescence emission spectra were recorded from 420 to 600 nm after excitation at 395

575   nm with the Infinite M1000 plate reader (Tecan, Austria). Rh Bri2 BRICHOS T206W

576   monomers were diluted to 2 µmol L^{-1} by using 20 mmol L^{-1} NaPi containing 0.2 mmol L^{-1}

577   EDTA with different pH in the final samples in the range of 6.3–8.0. For tryptophan

578   fluorescence measurements, samples were prepared in duplicates with a volume of 150 µL.

579   Samples were excited at 280 nm (5 µm bandwidth) and fluorescence emission from 300–400

580   nm (10 µm bandwidth, 1 nm step interval) was recorded on black polystyrene flat-bottom 96-

581   well plates (Costar) using a spectrofluorometer (Tecan Saphire 2). For the final fluorescence

582   intensities, the results were corrected by subtracting the background fluorescence of the

583   buffer.

584

585   **Transmission electron microscopy imaging of rh Bri2 BRICHOS D148N oligomers and**

586   **single particle processing**

18

587   Rh Bri2 BRICHOS D148N oligomers after SEC isolation were immediately stored on ice

588   followed by grid preparation. Aliquots (4 µL) were adsorbed onto glow-discharged

589   continuous carbon-coated copper grids (400 mesh, Analytical Standards) for one min. The

590   grids were subsequently blotted with filter paper, washed with two drops of milli-Q water,

591   and negatively stained with one drop of 2% (w/v) uranyl acetate for 45 s before final blotting

592   and air-drying. The sample was imaged using a Jeol JEM2100F field emission gun

593   transmission electron microscope (Jeol, Japan) operating at 200 kV. Single micrographs for

594   evaluating the quality of the sample were recorded on a Tietz 4k × 4k CCD camera, TVIPS

595   (Tietz Video and Image Processing Systems, GmbH, Gauting, Germany) at magnification

596   of× 85 200 (1.76Å per pixel) and 1.0–2.8 µm defocus. A total of 16 micrographs were

597   recorded for single particle analysis. All 16 micrographs were imported to EMAN2 (version

598   2.3) for further processing(70). After importing and estimating defocus with e2evalimage.py,

599   single particles in different orientations were selected from the images using e2boxer.py in

600   manual mode (11 094 particles, after one more manual selection, 10 223 particles were left).

601   For each image, the contrast transfer function (CTF) parameters were estimated on boxed out

602   regions (containing particles, 168×168) using e2ctf.auto.py program. A reference-free 2D

603   classification based on the selected 10 223 phase-flipped particles (low-pass filtered to 20 Å)

604   was performed using e2refine2d.py. The 2D classes show an approximate 2-fold symmetry,

605   which is consistent with both the results of rh wildtype Bri2 BRICHOS oligomer and the

606   biochemical data. Generated 2D classes were used as the input for building the 3D initial

607   model using e2initialmodel.py. 3D refinement was performed in several rounds using

608   e2refine_easy.py applying D2 symmetry aiming at a final resolution of 15 Å. The first two

609   rounds of 3D refinements were performed with pixel size of 3.52 Å after binning the data by

610   a linear factor 2. In the last round of refinement, the data was resampled to 2.464 Å per pixel.

611   The final map from the first round of refinements was used as model in the second, and the

612   final map from the second round of refinements was used as model in the third. The

613   resolution was determined based on a Fourier shell correlation (FSC) value of 0.143(71),

614   following the gold standard FSC procedure implemented in EMAN2(72).

615

616   **BRICHOS and Aβ42 monomer interaction monitored by surface plasmon resonance**

617   Aβ42 monomers were immobilized by amine coupling onto flowcell 4 on a CM5 sensor chip

618   (GE Healthcare) using a BIAcore 3000 instrument (BIAcore AB). A reference surface was

619   prepared on flowcell 3 using the same coupling protocol but without protein injected. The

620   immobilization was performed at a flow rate of 20 μL min^{-1} with 20 mmol L^{-1} sodium

621   phosphate pH 8.0 containing 0.2 mmol L^{-1} EDTA as running buffer, and the other details

622   were set according to the manufacturer's instructions. After immobilization with a final

623   reponse level of 727 RU, the flow-cells were stabilized over night in running buffer (10

624   mmol L^{-1} HEPES pH 7.5 containing 150 mmol L^{-1} NaCl and 0.2 mmol L^{-1} EDTA) at a flow

625   rate of 20 μL min^{-1}. For binding analysis, 25 μmol L^{-1} rh wildtype proSP-C BRICHOS or the

626   D105N mutant in 10 mmol L^{-1} HEPES pH 7.5 containing 150 mmol L^{-1} NaCl and 0.2 mmol

627   L^{-1} EDTA were injected in over the chip surfaces at 25°C at a flow rate of 20 μL min^{-1} for 3

628   min, respectively. 10 mmol L^{-1} NaOH was used for further chip surface regeneration. For

629   kinetic analysis, different concentrations of rh proSP-C BRICHOS D105N mutant in running

630   buffer, *i.e.* 0, 1.56, 3.13, 6.25, 12.5, 25, 50 and 100 μmol L^{-1}, were individually injected in

631   over the chip surfaces at 25°C at a flow rate of 20 μL min^{-1}. 30 mmol L^{-1} NaOH was used for

632   further chip surface regeneration. In all experiments, the response from the blank surface was

633   subtracted from the immobilized surface response, the baselines of the sensorgrams were

634   adjusted to zero and buffer spikes were excluded.

635

636   Steady state apparent affinities for rh proSP-C BRICHOS D105N mutant to immobilised

637   Aβ42 monomers were estimated by plotting the maximum binding response versus

638   BRICHOS concentrations. The baseline of the sensorgrams were adjusted to zero and buffer

639   spikes were excluded for global fits to reflect the binding affinity. Since the response signals

640   of the two lowest protein concentrations (*i.e.,* 1.56 and 3.13 μmol L^{-1}) used in kinetic analysis

641   were too weak, only sensorgrams obtained from rh proSP-C BRICHOS D105N mutant

642   ranging from 6.25 μmol L^{-1} to 100 μmol L^{-1} were included in the global fits. The dissociation

643   was globally fitted to a biexponential model as described by Eq. (**1**)(28, 73):

644    $R(t) = R_1(xe^{-k_{d1}(t-t_1)} + (1-x)e^{-k_{d2}(t-t_1)})$ Eq. (**1**)

645   where R_1 is the response signal at the starting time for the dissociation phase t_1, and x is

646   between 0 and 1. k_{d1} and k_{d2} are the dissociation rate constants for the fast and slow

647   dissociation phases, respectively. The global fitted value k_{d2} was used to calculate the

648   apparent K_D value.

649   The association phase was fitted to Eq. (**2**)(28):

650    $R(t) = R_f + (R_0 - R_f)e^{-k_{obs}t}$ Eq. (**2**)

651   where R_0 and R_f are the initial and final response signal of the association phase, respectively.

652   k_{obs} is the observed rate constant described by Eq. (**3**)(28, 73):

653    $$k_{obs} = ck_a + k_d \qquad \text{Eq. (3)}$$

654   where c is the protein concentration, k_a is the association rate constant, and k_d from this

655   analysis is related to secondary binding artifacts corresponding to k_{d1}. Linear regression was

656   used to determine k_a. The apparent K_D value was calculated as ratio of the dissociation rate

657   constant and association rate constant.

658

659   **Aβ42 monomer preparation and ThT assay**

660   Recombinant Met-Aβ(1–42), here referred to as Aβ42, was produced in BL21*(DE3) pLysS

661   *E. coli* (B strain) cells and purified by ion exchange(32). The purified Aβ42 peptides were

662   lyophilized and re-dissolved in 20 mmol L^{-1} Tris pH 8.0 with 7 mol L^{-1} Gdn-HCl, and the

663   monomers were isolated in 20 mmol L^{-1} sodium phosphate pH 8.0 with 0.2 mmol L^{-1} EDTA

664   by a Superdex 30 column 26/600 (GE Healthcare, UK). The concentration of monomeric

665   Aβ42 was calculated with using an extinction coefficient of 1 424 M^{-1} cm^{-1} for (A$_{280}$−A$_{300}$).

666   For Aβ42 fibrillization kinetics analysis, 20 µL solution containing 10 µmol L^{-1} ThT, 3 µmol

667   L^{-1} Aβ42 monomer and different concentrations of rh BRICHOS at molar ratios 0, 10, 30, 50,

668   70 or 100 % (relative to Aβ42 monomer molar concentration), were added to each well of

669   half-area 384-well microplates with clear bottom (Corning Glass 3766, USA), and incubated

670   at 37°C under quiescent conditions. The ThT fluorescence was recorded using a 440 nm

671   excitation filter and a 480 nm emission filter using a microplate reader (FLUOStar Galaxy

672   from BMG Labtech, Offenberg, Germany). For Aβ42 seeds preparation, 3 µmol L^{-1} Aβ42

673   monomers were incubated for about 20 h at 37°C, and the fibrils were then sonicated in a

674   water bath for 3 min. For seeding of Aβ42 fibrillization, 20 µL solution containing 10 µmol

675   L^{-1} ThT, 3 µmol L^{-1} Aβ42, different concentrations of rh BRICHOS at 0, 10, 50, 70 and

676   100 %, and 0.6 µmol L^{-1} seeds (calculated from the original Aβ42 monomer concentration)

677   were added at 4°C to each well in triplicate of 384-well microplates with clear bottom

678   (Corning Glass 3766, USA) and immediately incubated at 37°C under quiescent conditions.

679   The elongation rate constant k_+ in the presence of rh BRICHOS was calculated from the

680   highly seeded experiments. The initial slope of the concave aggregation traces was

681   determined by a linear fit of the first ~20 min traces. For all the experiments, aggregation

682   traces were normalized and averaged using four or three replicates, and data defining one

21

683   dataset was recorded from the same plate at the same time, and all the ThT data was from the

684   same batch of Aβ42 peptide.

685

686   **Analysis of Aβ42 aggregation kinetics**

687   Fibrillization traces of Aβ42 with and without different concentrations of rh BRICHOS were

688   fitted to a sigmoidal equation Eq. (**4**)(32, 33), where the half time $\tau_{1/2}$ and the maximal

689   growth rate r_{max} were extracted:

690    $F = F_0 + A/(1 + \exp[r_{max}(\tau_{1/2} - t)])$ Eq. (**4**)

691   where A the amplitude and F_0 the base value.

692

693   To dissect the molecular mechanism underlying BRICHOS counteracting Aβ42 aggregation,

694   the fibrillization traces were globally fitted by Eq. (**5**)(27):

$$\frac{M(t)}{M(\infty)} = 1 - \left(\frac{B_+ + C_+}{B_+ + C_+ \cdot \exp(\kappa t)} \cdot \frac{B_- + C_+ \cdot \exp(\kappa t)}{B_- + C_+} \right)^{\frac{k_\infty^2}{\kappa \tilde{k}_\infty}} \cdot \exp(-k_\infty t)$$ Eq. (**5**)

695   where $M(t)$ is the total fibril mass concentration, and the intermediate coefficients are

696   functions of λ and κ, and n_C and n_2 are the reaction orders for primary and secondary

697   nucleation, respectively:

$$C_\pm = \pm \lambda^2 /2/\kappa^2$$
$$k_\infty = \sqrt{2\kappa^2/(n_2(n_2 + 1)) + 2\lambda^2/n_C}$$
$$\tilde{k}_\infty = \sqrt{k_\infty^2 - 4C_+ C_- \kappa^2}$$
$$B_\pm = (k_\infty \pm \tilde{k}_\infty)/2/\kappa$$
$$\lambda = \sqrt{2 \cdot k_+ k_n \cdot m(0)^{n_C}}$$
$$\kappa = \sqrt{2 \cdot k_+ k_2 \cdot m(0)^{n_2+1}}$$

698   The microscopic rate constants k_n, k_+, and k_2 are for primary nucleation, elongation, and

699   secondary nucleation, respectively. The kinetic data were globally fitted to Eq. (**5**), where the

700   fits were partially constrained with one fitting parameter held to a constant value, resulting in

701   that only one rate constant (k_n, k_+ or k_2) is the sole fitting parameter(32, 33). To investigate

702   the generation of nucleation units, according to the nucleation rate $r_n(t)$(27):

703    $$r_n(t) = k_n m(t)^{n_C} + k_2 M(t) m(t)^{n_2},$$

704 the total number of nucleation units was calculated by integrating the nucleation rate $r_n(t)$

705 over the reaction.

706

Immunogold staining of Aβ42 fibrils and transmission electron microscopy analysis

708 Five μmol L^{-1} Aβ42 monomer was incubated at 37°C with 100% rh wildtype proSP-C

709 BRICHOS and the D105N mutant overnight, and the fibrils were collected at 4°C by

710 centrifugation for 1 h at 22 000×g. The fibrils were gently resuspended in 20 μL 1×TBS, of

711 which 2 μL were applied to carbon coated copper grids, and incubated for about 5 min.

712 Excess solution was removed and the girds were blocked by incubation in 1% BSA in 1×TBS

713 for 30 min, followed by 3×10 min washing by 1×TBS. The grids were then incubated with

714 polyclonal antibody against human proSP-C (SFTPC) (1:200 dilution, Atlas Antibodies)

715 overnight at 4°C, and washed 3×10 min with 1×TBS. Finally, the grids were incubated with

716 anti-rabbit IgG-gold coupled to 20 nm gold particles (1:40 dilution, BBI Solutions) for 2 h at

717 room temperature, and washed 5×10 min with 1×TBS. Excess solution was removed, and 2

718 μL of 2.5% uranyl acetate was added to each grid (kept about 20 s). Excess solution was

719 removed, and the grids were air-dried at room temperature, and analysed by transmission

720 electron microscopy (TEM, Jeol JEM2100F at 200 kV).

721

Electrophysiological recordings

723 All the animal experiments were carried out in accordance with the ethical permit granted by

724 Norra Stockholm's Djurförsöksetiska Nämnd (dnr N45/13). C57BL/6 mice of either sex

725 (postnatal days 14–23, supplied from Charles River, Germany) were used in the experiments.

726 Before sacrificed, all the mice were anaesthetized deeply using isoflurane.

727

728 The brain was dissected out and placed in modified ice-cold ACSF (artificial cerebrospinal

729 fluid). The ACSF contained 80 mmol L^{-1} NaCl, 24 mmol L^{-1} NaHCO$_3$, 25 mmol L^{-1} glucose,

730 1.25 mmol L^{-1} NaH$_2$PO$_4$, 1 mmol L^{-1} ascorbic acid, 3 mmol L^{-1} NaPyruvate, 2.5 mmol L^{-1}

731 KCl, 4 mmol L^{-1} MgCl$_2$, 0.5 mmol L^{-1} CaCl$_2$ and 75 mmol L^{-1} sucrose. Horizontal sections

732 (350 μm thick) of the ventral hippocampi from both hemispheres were sliced with a Leica

733 VT1200S vibratome (Microsystems, Sweden). The sections were immediately transferred to

734 a submerged incubation chamber containing standard ACSF: 124 mmol L^{-1} NaCl, 30 mmol

735 L^{-1} NaHCO$_3$, 10 mmol L^{-1} glucose, 1.25 mmol L^{-1} NaH$_2$PO$_4$, 3.5 mmol L^{-1} KCl, 1.5 mmol L^{-1}

736 MgCl$_2$ and 1.5 mmol L^{-1} CaCl$_2$. The chamber was held at 34°C for at least 20 min after

737   dissection and it was subsequently cooled to room temperature (~22°C) for a minimum of 40

738   min. Proteins (Aβ42 and rh BRICHOS) were first added to the incubation solution for 15 min,

739   and then the slices were transferred to the interface-style recording chamber for extracellular

740   recordings. During the incubation, slices were supplied continuously with carbogen gas (5%

741   CO_2, 95% O_2) bubbled into the ACSF.

742

743   Recordings were performed with borosilicate glass microelectrodes in hippocampal area CA3,

744   pulled to a resistance of 3–5 MΩ, filled with ACSF and placed in stratum pyramidale. Local

745   field potentials (LFP, γ oscillations) were recorded at 32°C in an interface-type chamber

746   (perfusion rate 4.5 mL per minute) and elicited by applying kainic acid (100 nmol L^{-1}, Tocris).

747   The oscillations were stabilized for 20 min before any recordings. No Aβ42, rh Bri2

748   BRICHOS R221E species or combinations thereof were present in the recording chamber

749   either during γ oscillations stabilization, or during electrophysiological recordings. The

750   interface chamber recording solution contained 124 mmol L^{-1} NaCl, 30 mmol L^{-1} $NaHCO_3$,

751   10 mmol L^{-1} glucose, 1.25 mmol L^{-1} NaH_2PO_4, 3.5 mmol L^{-1} KCl, 1.5 mmol L^{-1} $MgCl_2$ and

752   1.5 mmol L^{-1} $CaCl_2$.

753

754   Interface chamber LFP recordings were carried out by a 4-channel amplifier/signal

755   conditioner M102 amplifier (Electronics lab, University of Cologne, Germany). The signals

756   were sampled at 10 kHz, conditioned using a Hum Bug 50 Hz noise eliminator (LFP signals

757   only; Quest Scientific, North Vancouver, BC, Canada), software low-pass filtered at 1 kHz,

758   digitized and stored using a Digidata 1322A and Clampex 9.6 software (Molecular Devices,

759   CA, USA).

760

761   Power spectral density plots (from 60 s long LFP recordings) were calculated using

762   Axograph X (Kagi, Berkeley, CA, USA) in averaged Fourier-segments of 8 192 points.

763   Oscillation power was calculated from the integration of the power spectral density from 20

764   to 80 Hz.

765

766   **Statistics and reproducibility**

767   The electrophysiological data is presented as means ± standard errors of the means. Prior

768   statistical analysis all the data was subjected to outlier determination and removal with the

769   ROUT method (Q = 1%) followed by D'Agostino & Pearson omnibus normality test. Based

770   on the previous experience with the outliers and overall sample behaviour, sample size was

771   determined based on previous studies performed in an interface-type chamber(27, 32, 33, 47,

772   74, 75). Each experimental round was performed with parallel controls (Control KA and

773   Aβ42) from the same animal and randomized preparations (slices incubated with Aβ42 + rh

774   proSP-C BRICHOS D105N, + wildtype rh proSP-C BRICHOS, + rh Bri2-BRICHOS D148N

775   monomers or + wildtype rh Bri2-BRICHOS). For comparison purposes data from Control

776   KA and Aβ42 was pooled from interleaved slices recorded in these conditions. The number

777   of recorded slices per condition (at least from 3–5 mice) are shown in the corresponding

778   figure legend and source data file. Kruskal-Wallis test followed by Dunn's multiple

779   comparisons were carried out due to the non-parametric nature- or relatively small size of

780   some data. Comparison of the preventative efficacies of rh Bri2-BRICHOS D148N

781   monomers and rh proSP-C BRICHOS D105N was assessed with the Mann Whitney test.

782   Significance levels are * $p<0.05$, ** $p<0.01$, and ***$p<0.001$. The ThT assay data are

783   presented as means ± standard deviation, and the aggregation traces are averaged from four

784   or three replicates.

785   **References**

786   1.   Sipe JD, Benson MD, Buxbaum JN, Ikeda SI, Merlini G, Saraiva MJ, et al. Amyloid fibril
787   proteins and amyloidosis: chemical identification and clinical classification International
788   Society of Amyloidosis 2016 Nomenclature Guidelines. Amyloid. 2016;23(4):209-13.
789   2.   Landreh M, Sawaya MR, Hipp MS, Eisenberg DS, Wuthrich K, Hartl FU. The formation,
790   function and regulation of amyloids: insights from structural biology. J Intern Med.
791   2016;280(2):164-76.
792   3.   Bucciantini M, Giannoni E, Chiti F, Baroni F, Formigli L, Zurdo J, et al. Inherent toxicity
793   of aggregates implies a common mechanism for protein misfolding diseases. Nature.
794   2002;416(6880):507-11.
795   4.   Goldschmidt L, Teng PK, Riek R, Eisenberg D. Identifying the amylome, proteins
796   capable of forming amyloid-like fibrils. Proc Natl Acad Sci U S A. 2010;107(8):3487-92.
797   5.   Balchin D, Hayer-Hartl M, Hartl FU. In vivo aspects of protein folding and quality
798   control. Science. 2016;353(6294):aac4354.
799   6.   Soti C, Csermely P. Aging and molecular chaperones. Exp Gerontol.
800   2003;38(10):1037-40.
801   7.   Wolff S, Weissman JS, Dillin A. Differential scales of protein quality control. Cell.
802   2014;157(1):52-64.
803   8.   Hipp MS, Kasturi P, Hartl FU. The proteostasis network and its decline in ageing. Nat
804   Rev Mol Cell Biol. 2019.
805   9.   Sarparanta J, Jonson PH, Kawan S, Udd B. Neuromuscular Diseases Due to Chaperone
806   Mutations: A Review and Some New Results. Int J Mol Sci. 2020;21(4).

807   10.   Almeida-Souza L, Goethals S, de Winter V, Dierick I, Gallardo R, Van Durme J, et al.
808   Increased monomerization of mutant HSPB1 leads to protein hyperactivity in Charcot-
809   Marie-Tooth neuropathy. J Biol Chem. 2010;285(17):12778-86.
810   11.   Zhang YW, Thompson R, Zhang H, Xu H. APP processing in Alzheimer's disease. Mol
811   Brain. 2011;4:3.
812   12.   Westermark P, Andersson A, Westermark GT. Islet amyloid polypeptide, islet
813   amyloid, and diabetes mellitus. Physiol Rev. 2011;91(3):795-826.
814   13.   Häggqvist B, Näslund J, Sletten K, Westermark GT, Mucchiano G, Tjernberg LO, et al.
815   Medin: an integral fragment of aortic smooth muscle cell-produced lactadherin forms the
816   most common human amyloid. Proc Natl Acad Sci U S A. 1999;96(15):8669-74.
817   14.   Hedlund J, Johansson J, Persson B. BRICHOS - a superfamily of multidomain proteins
818   with diverse functions. BMC Res Notes. 2009;2:180.
819   15.   Sanchez-Pulido L, Devos D, Valencia A. BRICHOS: a conserved domain in proteins
820   associated with dementia, respiratory distress and cancer. Trends Biochem Sci.
821   2002;27(7):329-32.
822   16.   Willander H, Askarieh G, Landreh M, Westermark P, Nordling K, Keranen H, et al.
823   High-resolution structure of a BRICHOS domain and its implications for anti-amyloid
824   chaperone activity on lung surfactant protein C. Proc Natl Acad Sci U S A. 2012;109(7):2325-
825   9.
826   17.   Knight SD, Presto J, Linse S, Johansson J. The BRICHOS domain, amyloid fibril
827   formation, and their relationship. Biochemistry. 2013;52(43):7523-31.
828   18.   Buxbaum JN, Johansson J. Transthyretin and BRICHOS: The Paradox of
829   Amyloidogenic Proteins with Anti-Amyloidogenic Activity for Abeta in the Central Nervous
830   System. Front Neurosci. 2017;11:119.
831   19.   Martin L, Fluhrer R, Reiss K, Kremmer E, Saftig P, Haass C. Regulated intramembrane
832   proteolysis of Bri2 (Itm2b) by ADAM10 and SPPL2a/SPPL2b. J Biol Chem. 2008;283(3):1644-
833   52.
834   20.   Del Campo M, Hoozemans JJ, Dekkers LL, Rozemuller AJ, Korth C, Muller-Schiffmann
835   A, et al. BRI2-BRICHOS is increased in human amyloid plaques in early stages of Alzheimer's
836   disease. Neurobiol Aging. 2014;35(7):1596-604.
837   21.   Oskarsson ME, Hermansson E, Wang Y, Welsh N, Presto J, Johansson J, et al.
838   BRICHOS domain of Bri2 inhibits islet amyloid polypeptide (IAPP) fibril formation and toxicity
839   in human beta cells. Proc Natl Acad Sci U S A. 2018;115(12):E2752-E61.
840   22.   Vidal R, Revesz T, Rostagno A, Kim E, Holton JL, Bek T, et al. A decamer duplication in
841   the 3' region of the BRI gene originates an amyloid peptide that is associated with dementia
842   in a Danish kindred. Proc Natl Acad Sci U S A. 2000;97(9):4920-5.
843   23.   Vidal R, Frangione B, Rostagno A, Mead S, Revesz T, Plant G, et al. A stop-codon
844   mutation in the BRI gene associated with familial British dementia. Nature.
845   1999;399(6738):776-81.
846   24.   Willander H, Presto J, Askarieh G, Biverstal H, Frohm B, Knight SD, et al. BRICHOS
847   domains efficiently delay fibrillation of amyloid beta-peptide. J Biol Chem.
848   2012;287(37):31608-17.
849   25.   Nerelius C, Gustafsson M, Nordling K, Larsson A, Johansson J. Anti-amyloid activity of
850   the C-terminal domain of proSP-C against amyloid beta-peptide and medin. Biochemistry.
851   2009;48(17):3778-86.

852   26.   Scheidt T, Lapinska U, Kumita JR, Whiten DR, Klenerman D, Wilson MR, et al.
853   Secondary nucleation and elongation occur at different sites on Alzheimer's amyloid-beta
854   aggregates. Sci Adv. 2019;5(4):eaau3112.
855   27.   Cohen SIA, Arosio P, Presto J, Kurudenkandy FR, Biverstal H, Dolfe L, et al. A
856   molecular chaperone breaks the catalytic cycle that generates toxic Abeta oligomers. Nat
857   Struct Mol Biol. 2015;22(3):207-13.
858   28.   Leppert A, Tiiman A, Kronqvist N, Landreh M, Abelein A, Vukojevic V, et al. Smallest
859   Secondary Nucleation Competent Abeta Aggregates Probed by an ATP-Independent
860   Molecular Chaperone Domain. Biochemistry. 2021;60(9):678-88.
861   29.   Arosio P, Michaels TC, Linse S, Mansson C, Emanuelsson C, Presto J, et al. Kinetic
862   analysis reveals the diversity of microscopic mechanisms through which molecular
863   chaperones suppress amyloid formation. Nat Commun. 2016;7:10948.
864   30.   Poska H, Haslbeck M, Kurudenkandy FR, Hermansson E, Chen G, Kostallas G, et al.
865   Dementia-related Bri2 BRICHOS is a versatile molecular chaperone that efficiently inhibits
866   Abeta42 toxicity in Drosophila. Biochem J. 2016;473(20):3683-704.
867   31.   Hermansson E, Schultz S, Crowther D, Linse S, Winblad B, Westermark G, et al. The
868   chaperone domain BRICHOS prevents CNS toxicity of amyloid-beta peptide in Drosophila
869   melanogaster. Dis Model Mech. 2014;7(6):659-65.
870   32.   Chen G, Abelein A, Nilsson HE, Leppert A, Andrade-Talavera Y, Tambaro S, et al. Bri2
871   BRICHOS client specificity and chaperone activity are governed by assembly state. Nat
872   Commun. 2017;8(1):2081.
873   33.   Chen G, Andrade-Talavera Y, Tambaro S, Leppert A, Nilsson HE, Zhong X, et al.
874   Augmentation of Bri2 molecular chaperone activity against amyloid-beta reduces
875   neurotoxicity in mouse hippocampus in vitro. Commun Biol. 2020;3(1):32.
876   34.   Poska H, Leppert A, Tigro H, Zhong X, Kaldmäe M, Nilsson HE, et al. Recombinant
877   Bri3 BRICHOS domain is a molecular chaperone with effect against amyloid formation and
878   non-fibrillar protein aggregation. Sci Rep. 2020;10(1):9817.
879   35.   Nogee LM, Dunbar AE, 3rd, Wert S, Askin F, Hamvas A, Whitsett JA. Mutations in the
880   surfactant protein C gene associated with interstitial lung disease. Chest. 2002;121(3
881   Suppl):20S-1S.
882   36.   Dolfe L, Tambaro S, Tigro H, Del Campo M, Hoozemans JJM, Wiehager B, et al. The
883   Bri2 and Bri3 BRICHOS Domains Interact Differently with Abeta42 and Alzheimer Amyloid
884   Plaques. J Alzheimers Dis Rep. 2018;2(1):27-39.
885   37.   Panteleev P, Tsarev A, Bolosov I, Paramonov A, Marggraf M, Sychev S, et al. Novel
886   Antimicrobial Peptides from the Arctic Polychaeta Nicomache minor Provide New Molecular
887   Insight into Biological Role of the BRICHOS Domain. Mar Drugs. 2018;16(11).
888   38.   Papot C, Massol F, Jollivet D, Tasiemski A. Antagonistic evolution of an antibiotic and
889   its molecular chaperone: how to maintain a vital ectosymbiosis in a highly fluctuating
890   habitat. Sci Rep. 2017;7(1):1454.
891   39.   Tasiemski A, Jung S, Boidin-Wichlacz C, Jollivet D, Cuvillier-Hot V, Pradillon F, et al.
892   Characterization and function of the first antibiotic isolated from a vent organism: the
893   extremophile metazoan Alvinella pompejana. PLoS One. 2014;9(4):e95737.
894   40.   Hughes AL. Evolution of the lung surfactant proteins in birds and mammals.
895   Immunogenetics. 2007;59(7):565-72.
896   41.   Buzsaki G. Rhythms of the brain. Oxford Oxford University Press; 2006.

42.   Yamamoto J, Suh J, Takeuchi D, Tonegawa S. Successful execution of working memory linked to synchronized high-frequency gamma oscillations. Cell. 2014;157(4):845-57.

43.   Ribary U, Ioannides AA, Singh KD, Hasson R, Bolton JP, Lado F, et al. Magnetic field tomography of coherent thalamocortical 40-Hz oscillations in humans. Proc Natl Acad Sci U S A. 1991;88(24):11037-41.

44.   Iaccarino HF, Singer AC, Martorell AJ, Rudenko A, Gao F, Gillingham TZ, et al. Gamma frequency entrainment attenuates amyloid load and modifies microglia. Nature. 2016;540(7632):230-5.

45.   Martorell AJ, Paulson AL, Suk HJ, Abdurrob F, Drummond GT, Guan W, et al. Multi-sensory Gamma Stimulation Ameliorates Alzheimer's-Associated Pathology and Improves Cognition. Cell. 2019;177(2):256-71.e22.

46.   Kurudenkandy FR, Zilberter M, Biverstal H, Presto J, Honcharenko D, Stromberg R, et al. Amyloid-beta-induced action potential desynchronization and degradation of hippocampal gamma oscillations is prevented by interference with peptide conformation change and aggregation. J Neurosci. 2014;34(34):11416-25.

47.   Andrade-Talavera Y, Chen G, Kurudenkandy FR, Johansson J, Fisahn A. Bri2 BRICHOS chaperone rescues impaired fast-spiking interneuron behavior and neuronal network dynamics in an AD mouse model in vitro. Neurobiol Dis. 2021:105514.

48.   Khurana R, Coleman C, Ionescu-Zanetti C, Carter SA, Krishna V, Grover RK, et al. Mechanism of thioflavin T binding to amyloid fibrils. J Struct Biol. 2005;151(3):229-38.

49.   Cohen SI, Vendruscolo M, Dobson CM, Knowles TP. From macroscopic measurements to microscopic mechanisms of protein aggregation. J Mol Biol. 2012;421(2-3):160-71.

50.   Arosio P, Vendruscolo M, Dobson CM, Knowles TP. Chemical kinetics for drug discovery to combat protein aggregation diseases. Trends Pharmacol Sci. 2014;35(3):127-35.

51.   Hawe A, Sutter M, Jiskoot W. Extrinsic fluorescent dyes as tools for protein characterization. Pharm Res. 2008;25(7):1487-99.

52.   Casals C, Johansson H, Saenz A, Gustafsson M, Alfonso C, Nordling K, et al. C-terminal, endoplasmic reticulum-lumenal domain of prosurfactant protein C - structural features and membrane interactions. FEBS J. 2008;275(3):536-47.

53.   Prasad H, Rao R. Amyloid clearance defect in ApoE4 astrocytes is reversed by epigenetic correction of endosomal pH. Proc Natl Acad Sci U S A. 2018;115(28):E6640-E9.

54.   Su Y, Chang PT. Acidic pH promotes the formation of toxic fibrils from beta-amyloid peptide. Brain Res. 2001;893(1-2):287-91.

55.   Poon S, Rybchyn MS, Easterbrook-Smith SB, Carver JA, Pankhurst GJ, Wilson MR. Mildly acidic pH activates the extracellular molecular chaperone clusterin. J Biol Chem. 2002;277(42):39532-40.

56.   Decker Y, Nemeth E, Schomburg R, Chemla A, Fulop L, Menger MD, et al. Decreased pH in the aging brain and Alzheimer's disease. Neurobiol Aging. 2021;101:40-9.

57.   Hagihara H, Catts VS, Katayama Y, Shoji H, Takagi T, Huang FL, et al. Decreased Brain pH as a Shared Endophenotype of Psychiatric Disorders. Neuropsychopharmacology. 2018;43(3):459-68.

58.   Letunic I, Khedkar S, Bork P. SMART: recent updates, new developments and status in 2020. Nucleic Acids Res. 2021;49(D1):D458-d60.

59.   Huang Y, Niu B, Gao Y, Fu L, Li W. CD-HIT Suite: a web server for clustering and comparing biological sequences. Bioinformatics. 2010;26(5):680-2.

60.   Mistry J, Chuguransky S, Williams L, Qureshi M, Salazar GA, Sonnhammer ELL, et al. Pfam: The protein families database in 2021. Nucleic Acids Res. 2021;49(D1):D412-d9.

61.   Eddy SR. Accelerated Profile HMM Searches. PLoS Comput Biol. 2011;7(10):e1002195.

62.   Poska H. In vitro and in vivo studies of molecular chaperone activity against fibrillar and non-fibrillar protein aggregation. Tallinn: Tallinn University; 2020.

63.   Katoh K, Rozewicki J, Yamada KD. MAFFT online service: multiple sequence alignment, interactive sequence choice and visualization. Brief Bioinform. 2019;20(4):1160-6.

64.   Crooks GE, Hon G, Chandonia JM, Brenner SE. WebLogo: a sequence logo generator. Genome Res. 2004;14(6):1188-90.

65.   Stamatakis A. RAxML-VI-HPC: maximum likelihood-based phylogenetic analyses with thousands of taxa and mixed models. Bioinformatics. 2006;22(21):2688-90.

66.   Letunic I, Bork P. Interactive Tree Of Life (iTOL) v4: recent updates and new developments. Nucleic Acids Res. 2019;47(W1):W256-w9.

67.   Kronqvist N, Sarr M, Lindqvist A, Nordling K, Otikovs M, Venturi L, et al. Efficient protein production inspired by how spiders make silk. Nat Commun. 2017;8:15504.

68.   Johansson H, Eriksson M, Nordling K, Presto J, Johansson J. The Brichos domain of prosurfactant protein C can hold and fold a transmembrane segment. Protein Sci. 2009;18(6):1175-82.

69.   Srere PA. Citrate-condensing enzyme-oxalacetate binary complex. Studies on its physical and chemical properties. J Biol Chem. 1966;241(9):2157-65.

70.   Tang G, Peng L, Baldwin PR, Mann DS, Jiang W, Rees I, et al. EMAN2: an extensible image processing suite for electron microscopy. J Struct Biol. 2007;157(1):38-46.

71.   Rosenthal PB, Henderson R. Optimal determination of particle orientation, absolute hand, and contrast loss in single-particle electron cryomicroscopy. J Mol Biol. 2003;333(4):721-45.

72.   Scheres SH, Chen S. Prevention of overfitting in cryo-EM structure determination. Nat Methods. 2012;9(9):853-4.

73.   Rahman MM, Zetterberg H, Lendel C, Härd T. Binding of human proteins to amyloid-β protofibrils. ACS Chem Biol. 2015;10(3):766-74.

74.   Balleza-Tapia H, Crux S, Andrade-Talavera Y, Dolz-Gaiton P, Papadia D, Chen G, et al. TrpV1 receptor activation rescues neuronal function and network gamma oscillations from Abeta-induced impairment in mouse hippocampus in vitro. Elife. 2018;7.

75.   Kurudenkandy FR, Zilberter M, Biverstål H, Presto J, Honcharenko D, Strömberg R, et al. Amyloid-β-induced action potential desynchronization and degradation of hippocampal gamma oscillations is prevented by interference with peptide conformation change and aggregation. J Neurosci. 2014;34(34):11416-25.

Acknowledgements

1002

Author contributions:

G.C., Y.A.T., X.Z., H.P., H.B., A.L., and N.K. performed experiments. S.H. and G.C. carried out bioinformatic analyses and visualization. G.C., Y.A.T., X.Z., H.B., H.P., A.A., N.K., A.R., H.H., P. K., A.F., and J.J. analysed the data. G.C. and J.J. conceived the study. G.C. and J.J. wrote the paper. All authors discussed the results and commented on the manuscript.

1008

Competing interests:

The authors declare no competing financial interests.

1011

Data and materials availability:

The density map of the Bri2 BRICHOS D148N oligomer have been deposited in the Electron Microscopy Data Bank (EMDB) under the accession code EMD-13005. All data and materials related to this paper are available from G.C. (gefei.chen@ki.se).

1016

1017

1018

1019

1020

1021

1022

1023

1024

1025

1026

1027

1028

1029

1030

1031

1032

1033

1034

1035

1036

1037

1038

1039

1040   **Figures**
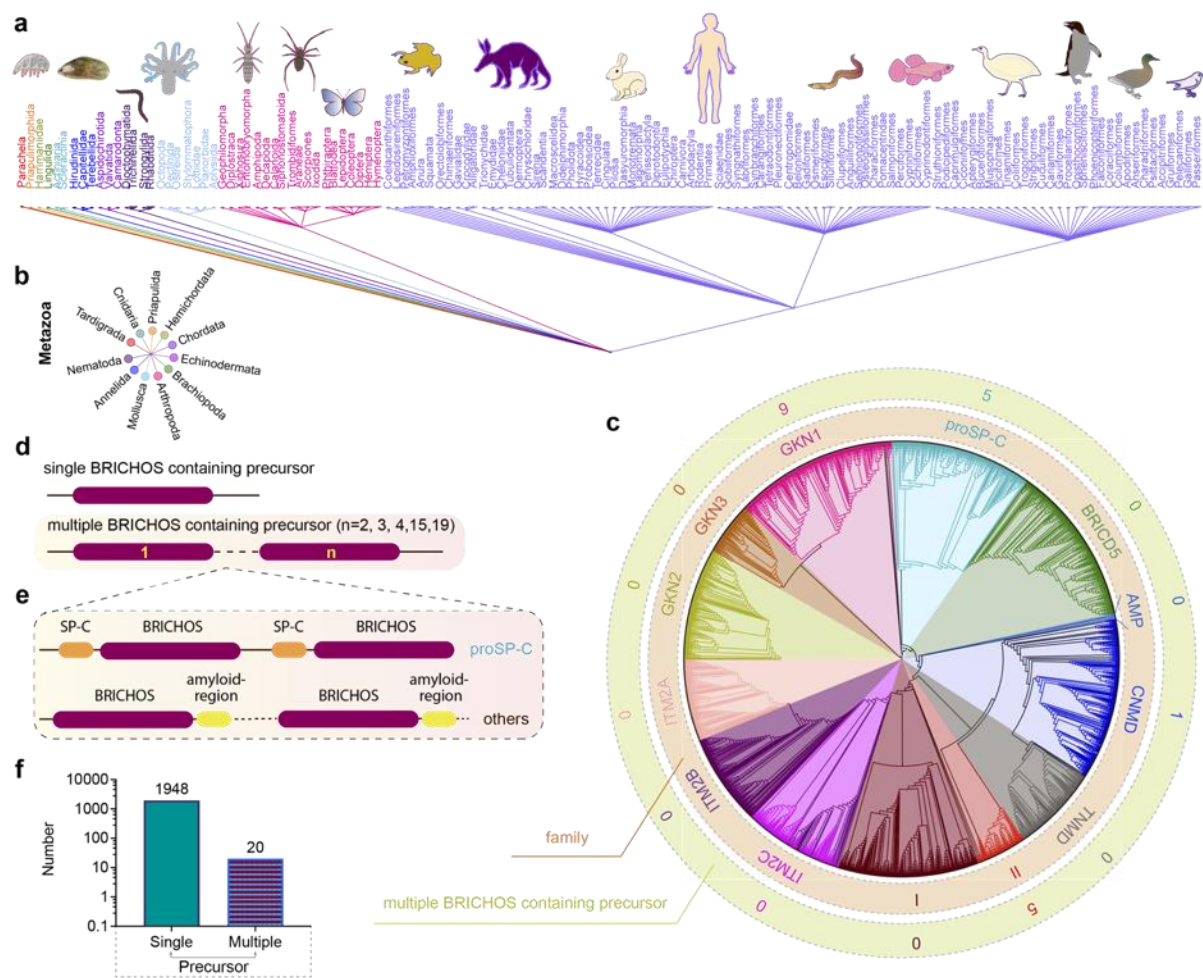
Fig. 1. Evolutionary analyses of the BRICHOS domain. (**a**) The common taxonomy tree for all species containing BRICHOS domain precursors. The 3 355 BRICHOS precursors are distributed in a broad range of species, including worms, insects to human, and which belong to eleven metazoan phyla (**b**). (**c**) The selected 2 019 BRICHOS domains are grouped into thirteen families (inner ring), with bootstraps shown in **Supplementary Figure 1**. The outer ring shows the number of cases of occurrence of multiple BRICHOS domains in the respective families. (**d**) Architecture of proproteins containing single and up to nineteen multiple BRICHOS domains. The detailed architectures for each case are shown in **Supplementary Figure 2**. (**e**) the multiple BRICHOS domains showed there are a few BRICHOS containing proproteins that contain multiple BRICHOS domains along with representatives of their corresponding amyloid-prone regions. The true domain size is not proportional to the schematic bar. (**f**) The number of proproteins that contain single or multiple BRICHOS domains. 1 948 out of 1 968 proproteins contain a single BRICHOS domain while the others contain multiple BRICHOS domains.

32

1056
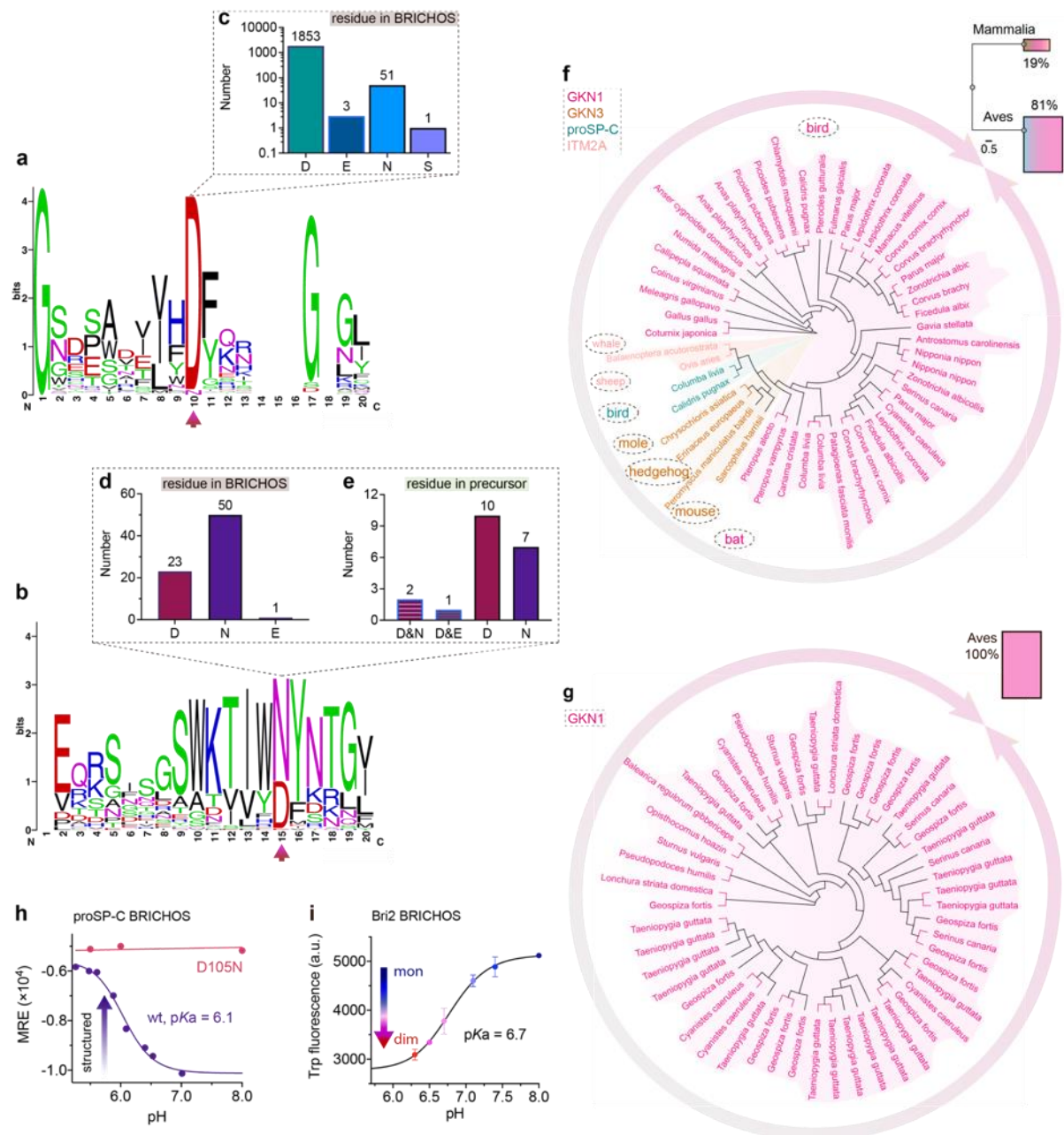
Fig. 2. BRICHOS domain sequence analysis and species distribution. (**a**) WebLogo representation of amino acid sequence alignments of the 1908 single BRICHOS domains, surrounding the conserved Asp (red arrow). The height of the amino acid stack represents the sequence conservation, while the height of symbols within each stack indicates the relative frequency of each residue and the total height of the letters is given in bits. (**b**) WebLogo representation as in panel (**a**) of sequence alignments of the 74 multiple BRICHOS domains. (**c**) The residue distribution at the position of the conserved Asp in single BRICHOS domains. (**d**) The residue distribution at the position of the conserved Asp in multiple BRICHOS domains. (**e**) The consistency of Asp or Asn, or the combination of Asp and Asn (or Glu) in individual multiple BRICHOS containing precursor. (**f**) Family and species distributions of

1067   cases that contain Asn in single BRICHOS domains. (**g**) Family and species distributions of

1068   cases that contain Asn in multiple BRICHOS domains. (**h**) pH-dependent structural changes

1069   of rh proSP-C BRICHOS variants monitored by CD, the details are shown in

1070   **Supplementary Figure 5b and c**. (**i**) pH-dependent transition of rh Bri2 BRICHOS

1071   monomers to dimers measured by Trp fluorescence, the details are shown in **Supplementary**

1072   **Figure 9b and c**.

1073

1074
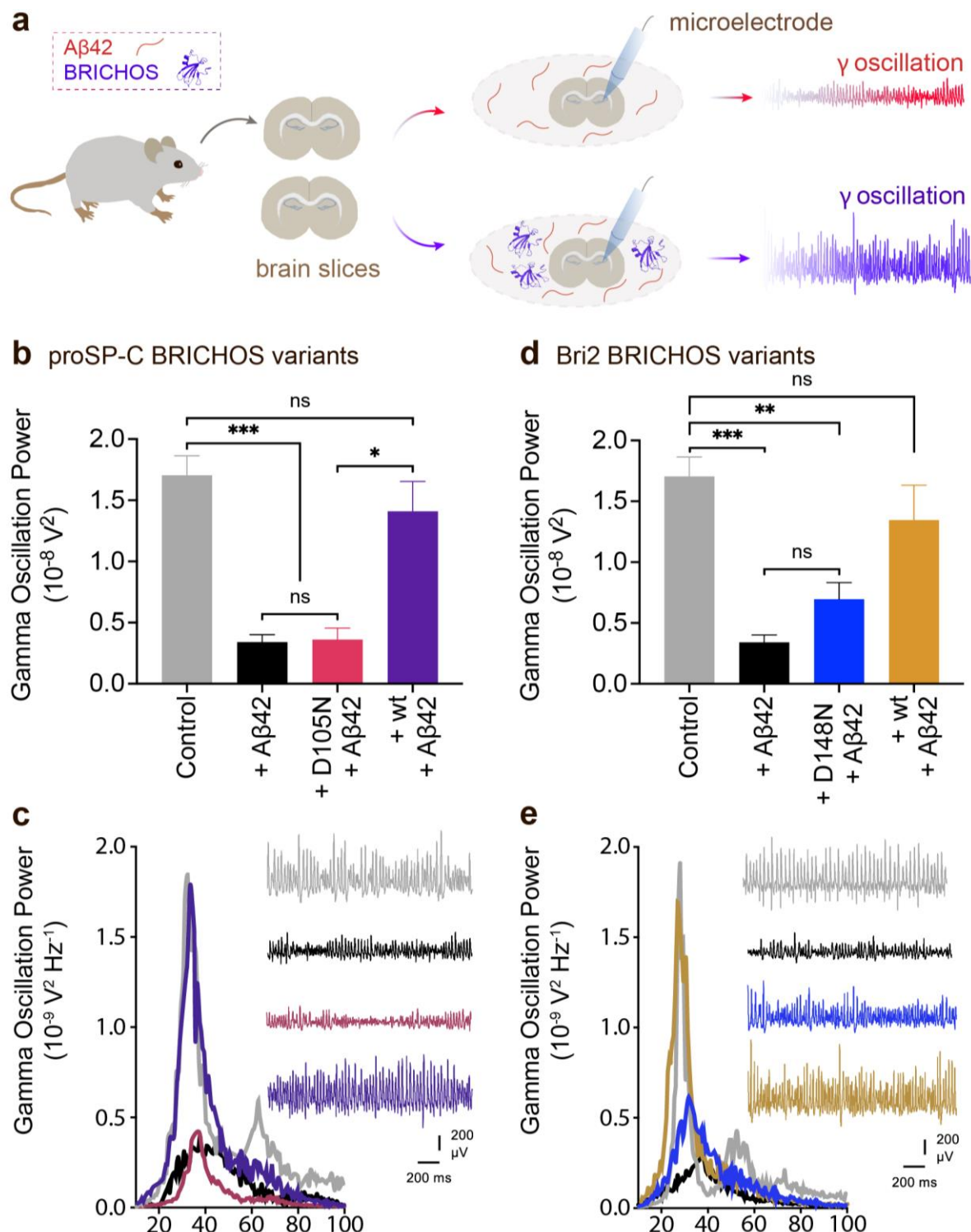
Fig. 3. Asp to Asn mutation reduces rh proSP-C BRICHOS and rh Bri2 BRICHOS capacity against Aβ42 neurotoxicity. (**a**) Schematic diagram of electrophysiological recordings. The hippocampal slices from wildtype C57BL/6 mice were preincubated either with 50 nmol L^{-1} Aβ42 alone or co-incubated with 100 nmol L^{-1} rh BRICHOS, and γ oscillations were then recorded in the CA3 area. (**b**) Summary plot of normalized γ oscillation power under control conditions (gray, n=20), after 15 min incubation with 50

1082 nmol L^{-1} Aβ42 (black, n=14), 50 nmol L^{-1} Aβ42 + 100 nmol L^{-1} D105N (red, n=9) or

1083 wildtype (purple, n=9) rh proSP-C BRICHOS. Example traces and example power spectra

1084 are shown with the same color coding in (**c**). (**d**) Summary plot of γ oscillation power under

1085 control conditions (gray, n=20), after 15 min incubation with 50 nmol L^{-1} Aβ42 (black, n=14),

1086 50 nmol L^{-1} Aβ42 + 100 nmol L^{-1} D148N monomeric (blue, n=11) or wildtype monomeric

1087 (yellow, n=8) rh Bri2 BRICHOS. Example traces and example power spectra are shown with

1088 the same color coding in (**e**). The data are reported as means ± standard errors of the means.

1089 ns, no significant difference, *$p < 0.05$, **$p < 0.01$, ***$p < 0.001$.

1090

1091

1092

1093
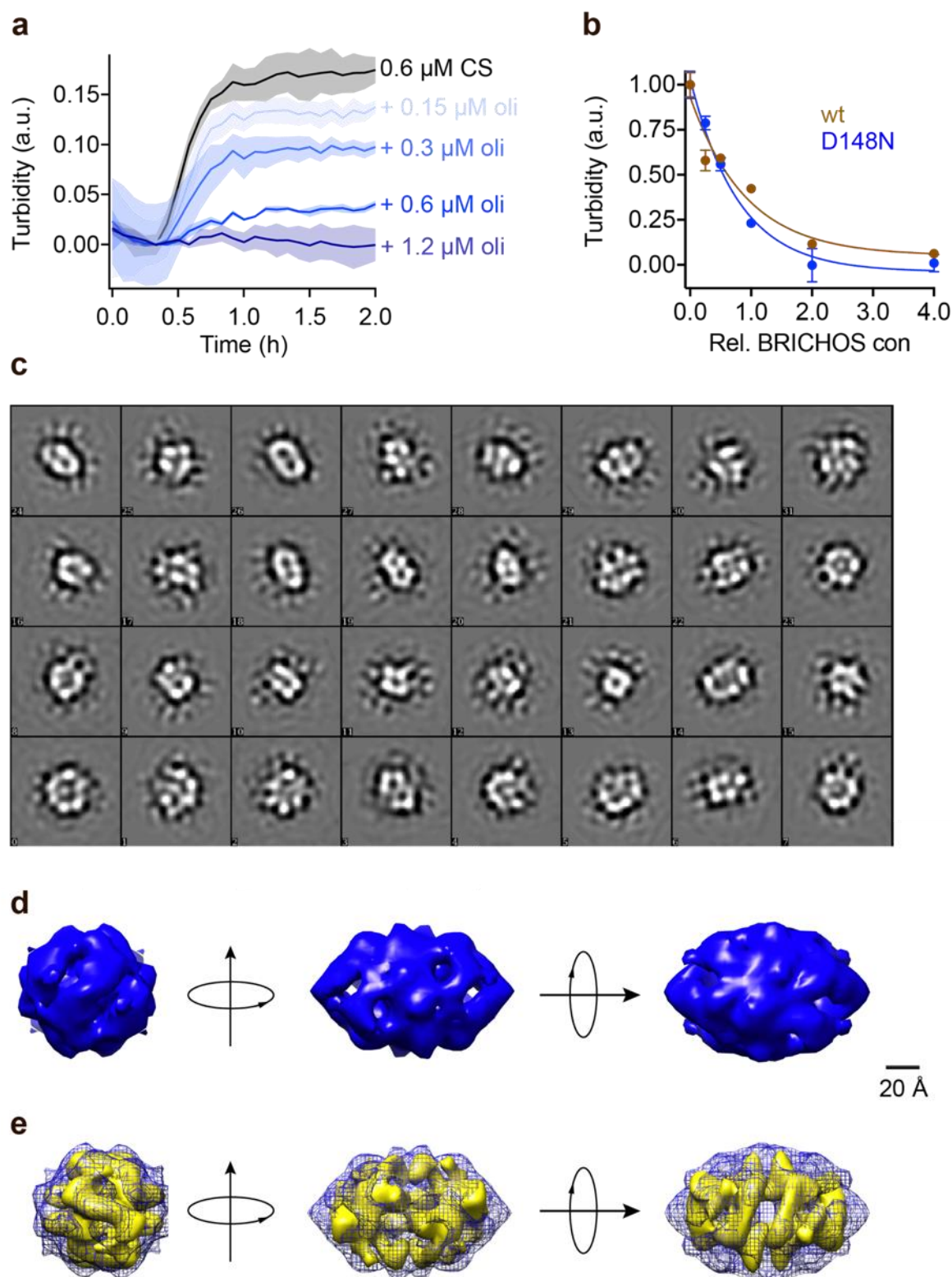
Fig. 4. Rh Bri2 BRICHOS D148N oligomer EM map and comparison with the wildtype oligomer 3D EM density map. (**a**) Kinetics of aggregation of 600 nmol L^{-1} citrate synthase (CS) at 45 °C alone (black), in the presence of 0.15, 0.3, 0.6 and 1.2 µmol L^{-1} rh Bri2 BRICHOS D148N oligomer. The different concentrations of the oligomers are shown with a blue gradient, which are labelled on the right of the traces. (**b**) Effects of rh Bri2 BRICHOS

37

1099   D148N and wildtype oligomers (data from ref [32]) on CS aggregation at different molar ratios

1100   (referred to monomeric subunits) of BRICHOS:CS. The data are presented as means ±

1101   standard deviations. (**c**) 2D classes of rh Bri2 BRICHOS D148N oligomers. Most class

1102   averages show an approximate 2-fold symmetry. (**d**) The three viewing directions are along

1103   the three different 2-fold axes (upper panel). The map of rh Bri2 BRICHOS D148N oligomer

1104   was based on 10 223 particles manually extracted from images recorded on a CCD detector

1105   with ×85 200 magnification and the voxel size of the map is 2.464 Å. The lower panel shows

1106   the 3D density map of rh Bri2 BRICHOS D148N oligomer with D2 symmetry (blue) and the

1107   volume fit in rh wildtype Bri2 BRICHOS oligomer (yellow, EMDB: 3918).

1108
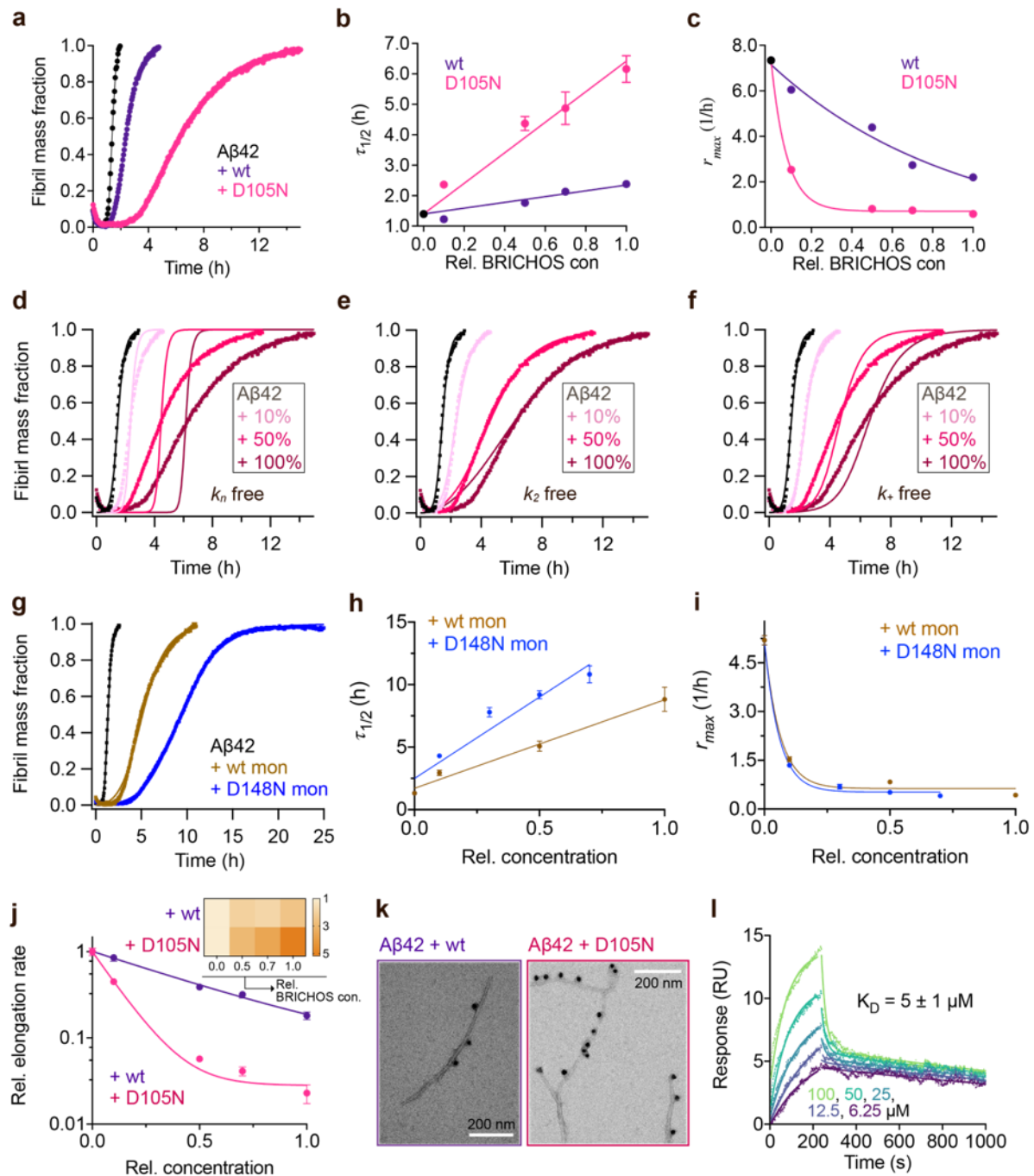
Fig. 5. Asp to Asn mutation changes rh proSP-C BRICHOS activity against Aβ42 fibril formation. (**a**) Activity comparison of 100% rh wildtype proSP-C BRICHOS (purple) and rh proSP-C BRICHOS D105N (red) against 3 µmol L^{-1} Aβ42 (black). Individual fits with combined rate constants $\sqrt{k_n k_+}$ and $\sqrt{k_+ k_2}$ as free fitting parameters of normalized and averaged aggregation traces (dots) are shown as solid lines. Values for $\tau_{1/2}$ (**b**) and r_{max} (**c**) extracted from sigmoidal fitting of Aβ42 aggregation traces in the presence of different concentrations of rh wildtype proSP-C BRICHOS (purple) or rh proSP-C BRICHOS D105N (red) as shown in (**d-f**) and (**Supplementary Figure 10a–c**). (**d–e**) Aggregation kinetics of 3

1118   µmol L^{-1} Aβ42 in the presence of rh proSP-C BRICHOS D105N at concentrations: 0 (black),

1119   10 (light red), 50 (red), or 100% (dark red) molar percentage referred to monomeric subunits

1120   relative to Aβ42 monomer. The global fits (solid lines) of the aggregation traces (crosses)

1121   were constrained such that only one single rate constant is the free fitting parameter,

1122   indicated in each panel. χ^2 values describing the quality of the fits: 18 for k_n free, 0.8 for k_2

1123   free and 3.2 for k_+ free. (**g**) Comparison of 50% rh wildtype Bri2 BRICHOS (yellow) and rh

1124   Bri2 BRICHOS D148N (blue) activities against 3 µmol L^{-1} Aβ42 (black). The solid lines are

1125   from individual fits with combined rate constants $\sqrt{k_n k_+}$ and $\sqrt{k_+ k_2}$ as free fitting

1126   parameters of normalized and averaged aggregation traces (dots). Values for $\tau_{1/2}$ (**h**) and r_{max}

1127   (**i**) extracted from the sigmoidal fitting of Aβ42 aggregation traces in the presence of

1128   different concentrations of rh wildtype Bri2 BRICHOS and the D148N mutant as shown in

1129   (**Supplementary Figure 10c–e**). (**j**) Elongation rates (k_+) determined from highly seeded

1130   aggregation kinetics in **Supplementary Figure 10d** and **e**. The inset shows the amount of

1131   toxic Aβ42 oligomers calculated with the relative elongation rates (k_+) and secondary

1132   nucleation rates (k_2) for either rh wildtype proSP-C BRICHOS or the D105N mutant. (**k**)

1133   Immuno-EM of BRICHOS bound to Aβ42 fibrils. Aβ42 was incubated with and without 100%

1134   molar ratio of rh wildtype proSP-C BRICHOS and the D105N mutant, respectively,

1135   overnight at 37°C. The samples were treated with a polyclonal antibody against human

1136   proSP-C and a gold-labelled secondary antibody, and characterized by TEM. The scale bars

1137   are 200 nm. (**l**) SPR sensorgrams of different concentrations (*i.e.,* 6.25, 12.5, 25, 50, and 100

1138   µmol L^{-1}) of rh proSP-C BRICHOS D105N interacting with immobilized Aβ42 monomers.

1139   The data were globally fitted for the association and disassociation phases, respectively, and

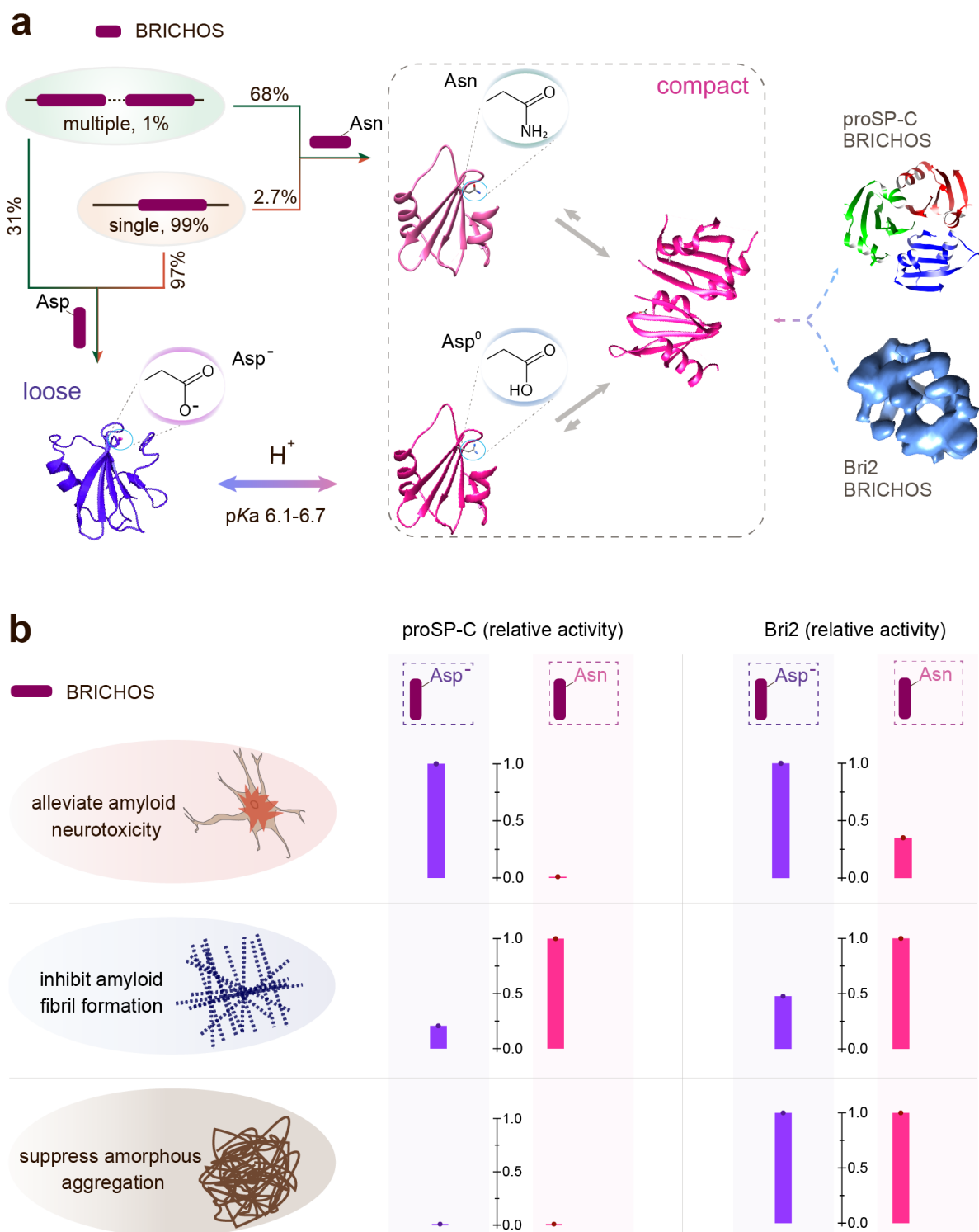1140   the apparent K_D was calculated.

1141

1142

Fig. 6. Schematic summary of BRICHOS activities depending on ionization state of its conserved Asp. (a) Asp and Asn in BRICHOS domains (single and multiple BRICHOS precursors account for 94% and 5%, and adopt "loose" and "compact" conformation, respectively. At neutral pH, the conserved Asp is ionized (Asp⁻) and BRICHOS presents an open structure (from ref[16]). At pH 6-7, the Asp is protonated and BRICHOS is more compact (PDB accession number 2YAD, from crystals prepared at pH 6.5[ref(16)]) and prone to

41

1150   dimerize, which could be mimicked by Asn present in some BRICHOS families. Eventually,

1151   proSP-C BRICHOS forms trimers (2YAD), while Bri2 BRICHOS forms larger oligomeric

1152   assemblies (EMD-3918). **(b)** The activities of BRICHOS are regulated by the conserved Asp;

1153   with its ionization form BRICHOS can efficient present anti-amyloid-induced neurotoxicity.

1154   Protonation of the Asp or replaced by Asn diminishes the activity for BRICHOS anti-

1155   amyloid-induced neurotoxicity, but oppositely, the capacity inhibiting amyloid fibril is

1156   significantly enhanced. After forming large oligomers, the general chaperone activity against

1157   amorphous aggregation is not obviously affected. The y-axis is the normalized activity with

1158   substrate alone as 0 and the higher activity from the wildtype species or the mutant as 1. For

1159   the neurotoxicity, the data used are from a ratio of 1:2 (substrate: BRICHOS) for proSP-C

1160   BRICHOS and 1:1 for Bri2 BRICHOS. For the activity against amyloid fibril formation, the

1161   data are from a ratio of 1:1 (substrate: BRICHOS) for proSP-C BRICHOS and 1:0.5 for Bri2

1162   BRICHOS. For the general chaperone activity against amorphous aggregation, the data used

1163   are from a ratio of 1:2.4 (substrate: BRICHOS), both for proSP-C BRICHOS and for Bri2

1164   BRICHOS.

1165

1166

1167

1168

1169

1170

1171

1172

1173

1174

1175

1176

1177

1178

1179

1180

1181

1182

1183

1184

Supplementary Figures

1185

1186

1187
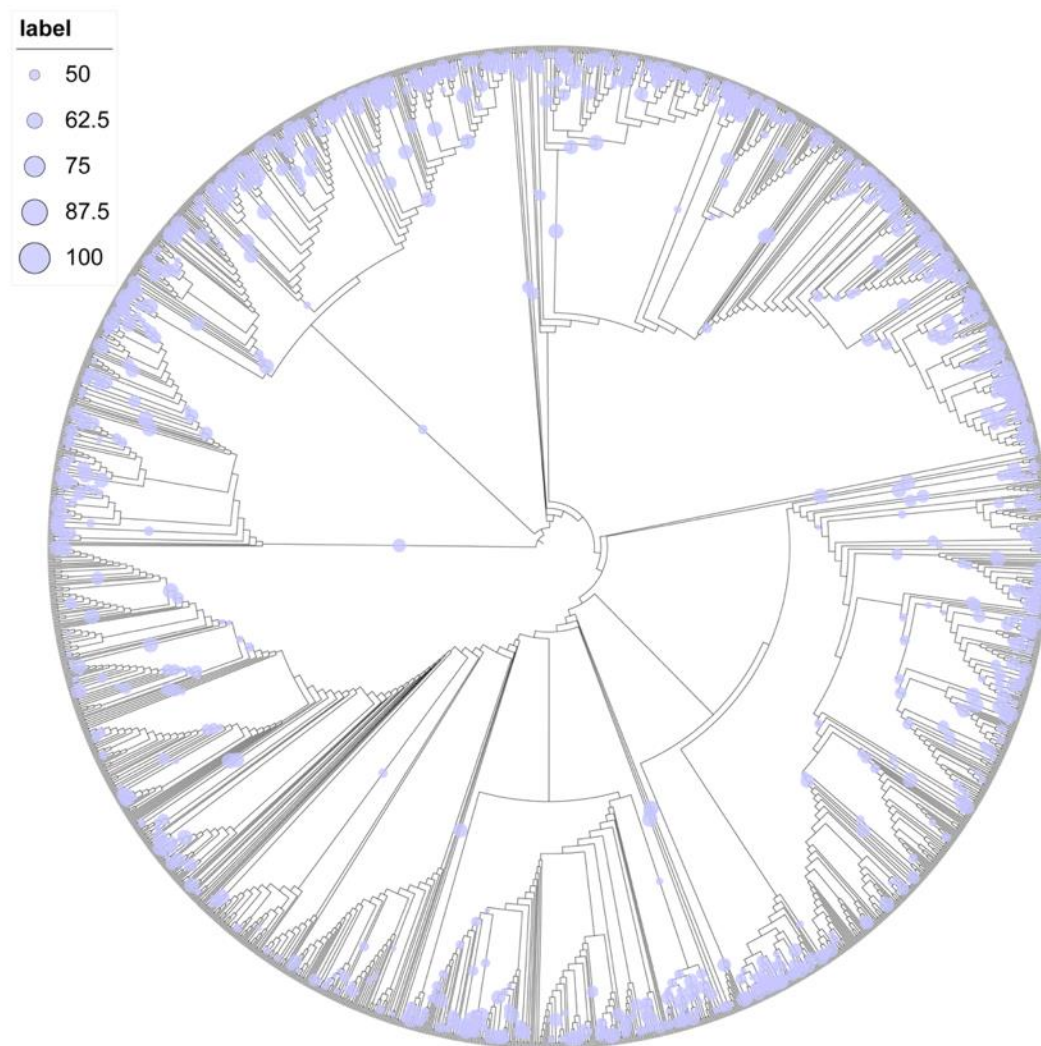
1188   **Fig. S1. Evolution of the molecular chaperone domain BRICHOS.** Phylogenetic tree of

1189   the 2 019 BRICHOS domains, which was grouped into thirteen families (**Fig. 1c**). The

1190   bootstraps larger than 50% are indicated by labels, where the sizes are proportional to the
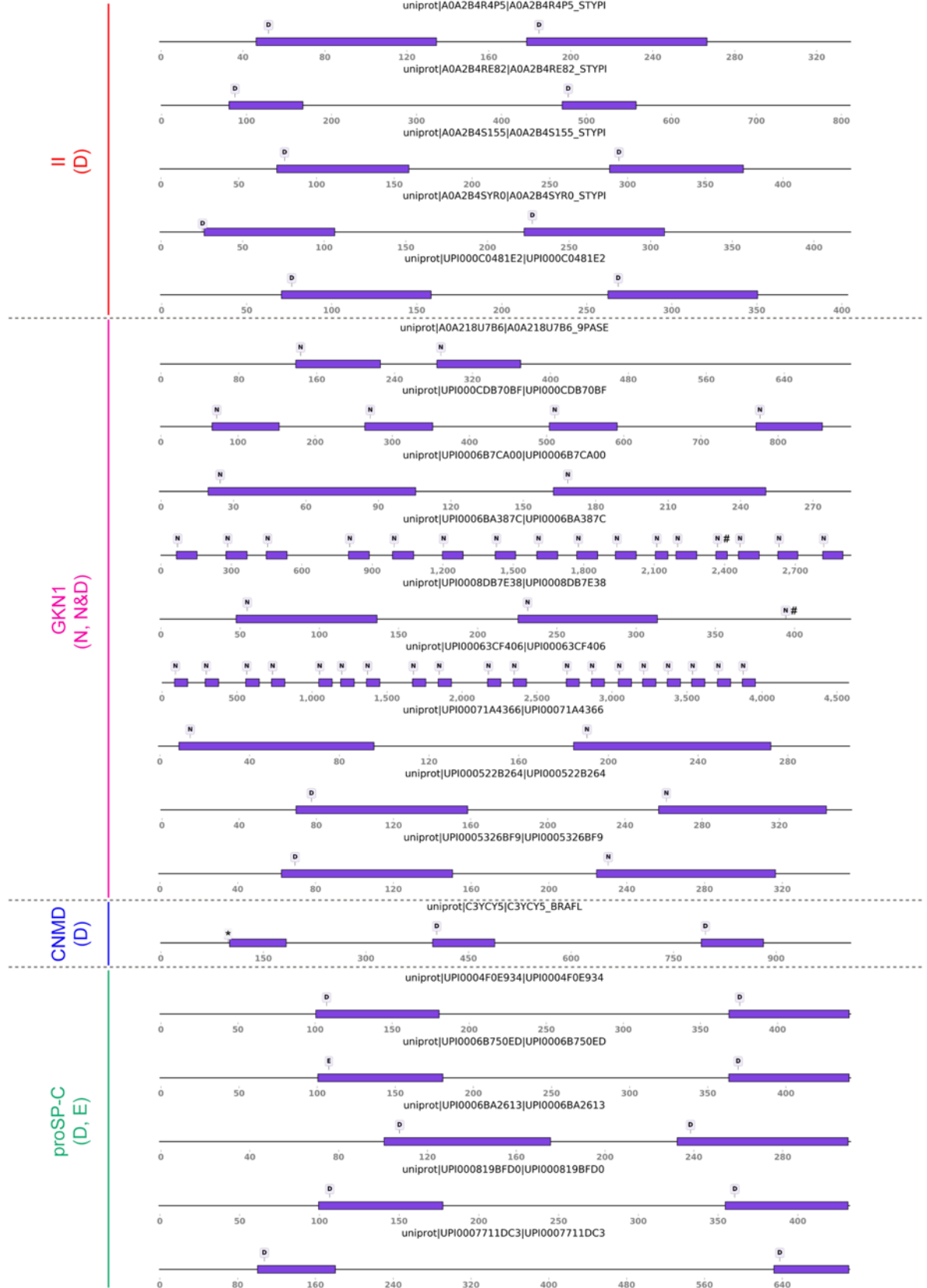
1191   bootstrap values.

Fig. S2. The architecture of proproteins containing multiple BRICHOS domains. The proproteins contain up to nineteen multiple, tandem BRICHOS domains (multi-BRICHOS). The architecture is generally shown in **Figure 1d**. The uniport accession number is shown

1196   over each corresponding cartoon. The length of the bar is not proportional to the size of the

1197   BRICHOS domain from different precursors. # refers to the C-terminally truncated, and *

1198   indicated the N-terminally truncated.

1199
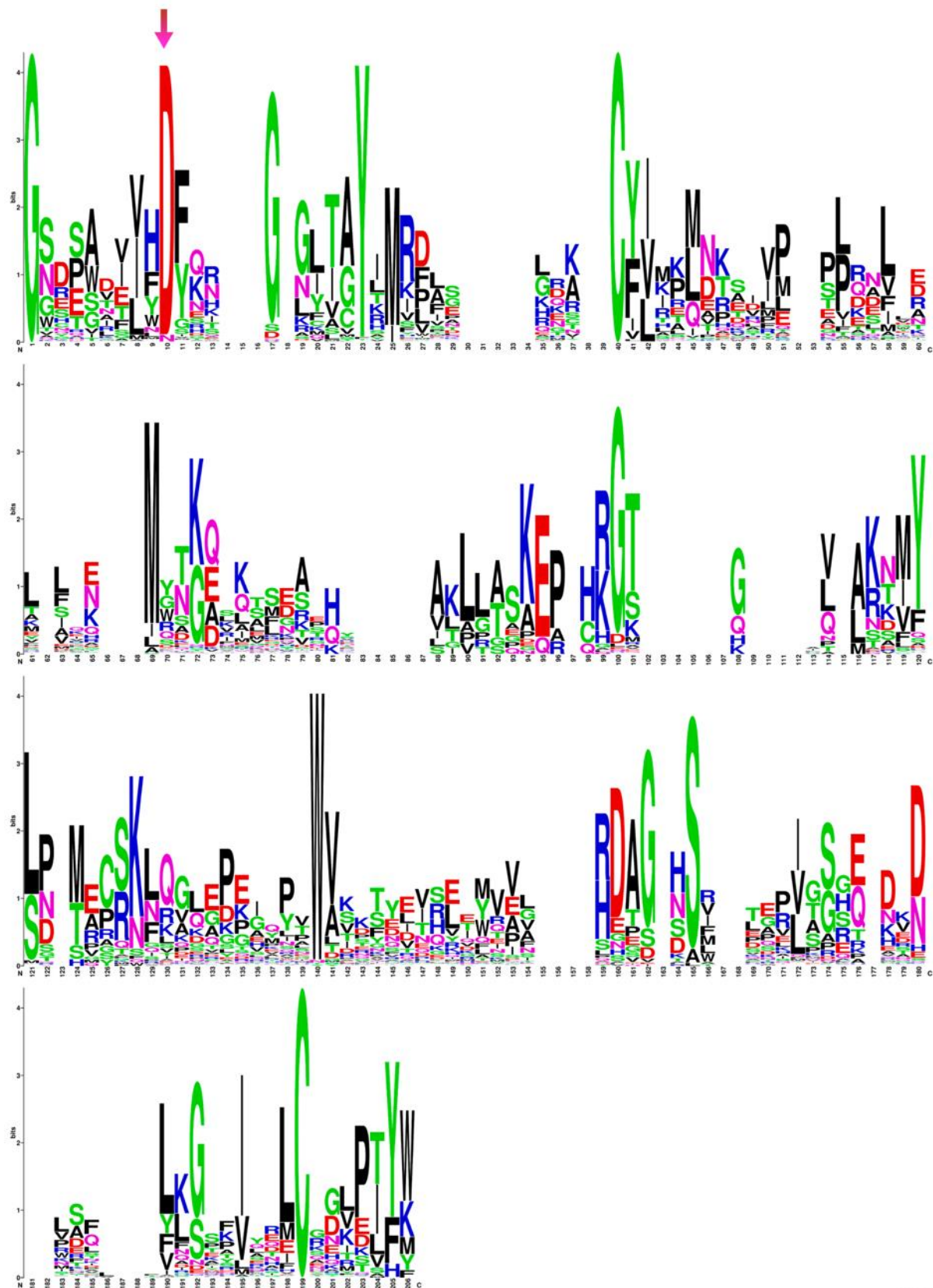
Fig. S3. WebLogo representation of the 1 908 single BRICHOS domains. The height of the residue stack implies the sequence conservation, while the height of symbols within the

46

1203   stack indicates the relative frequency of each residue. The arrow marks the conserved Asp

1204   residue.

1205

1206

1207
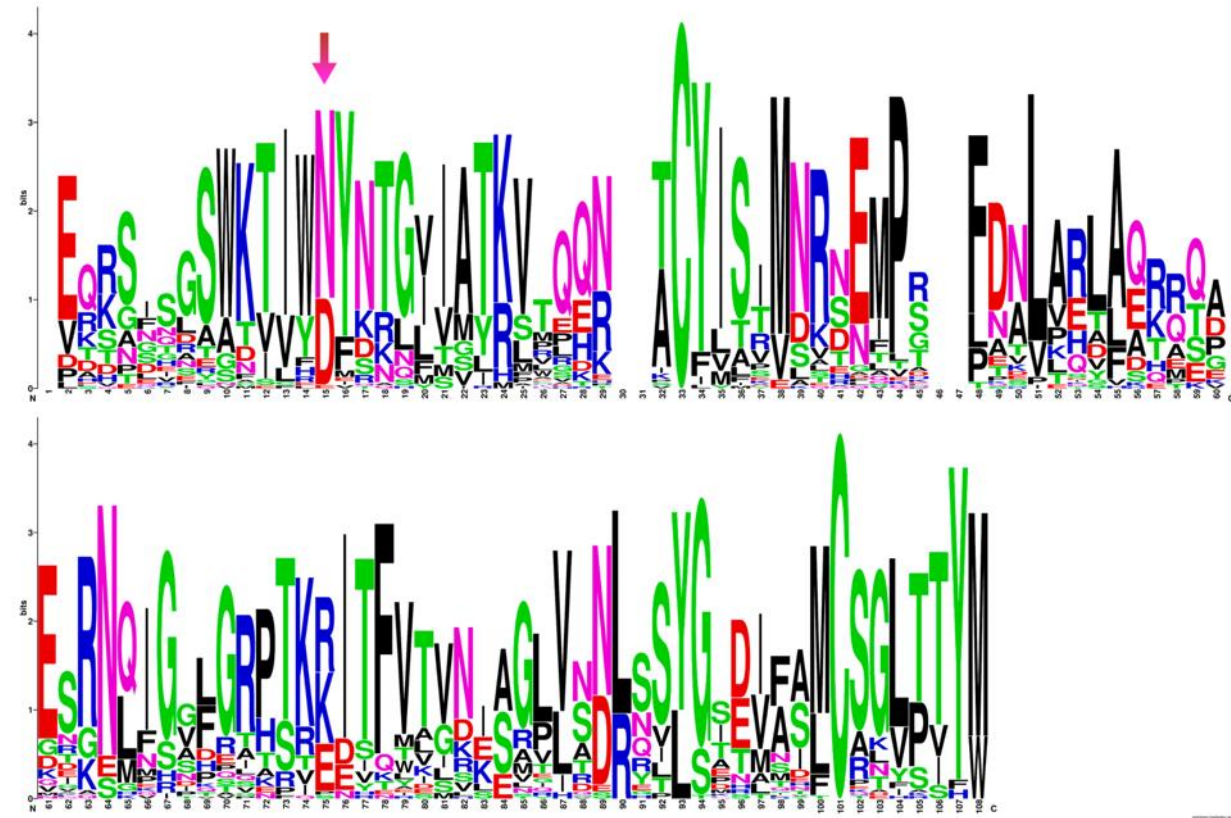
1208
1209   **Fig. S4. WebLogo representation of the 74 multiple BRICHOS domains.** The height of

1210   the residue stack implies the sequence conservation, while the height of symbols within the

1211   stack indicates the relative frequency of each residue. The arrow marks the conserved Asp

1212   residue.

47
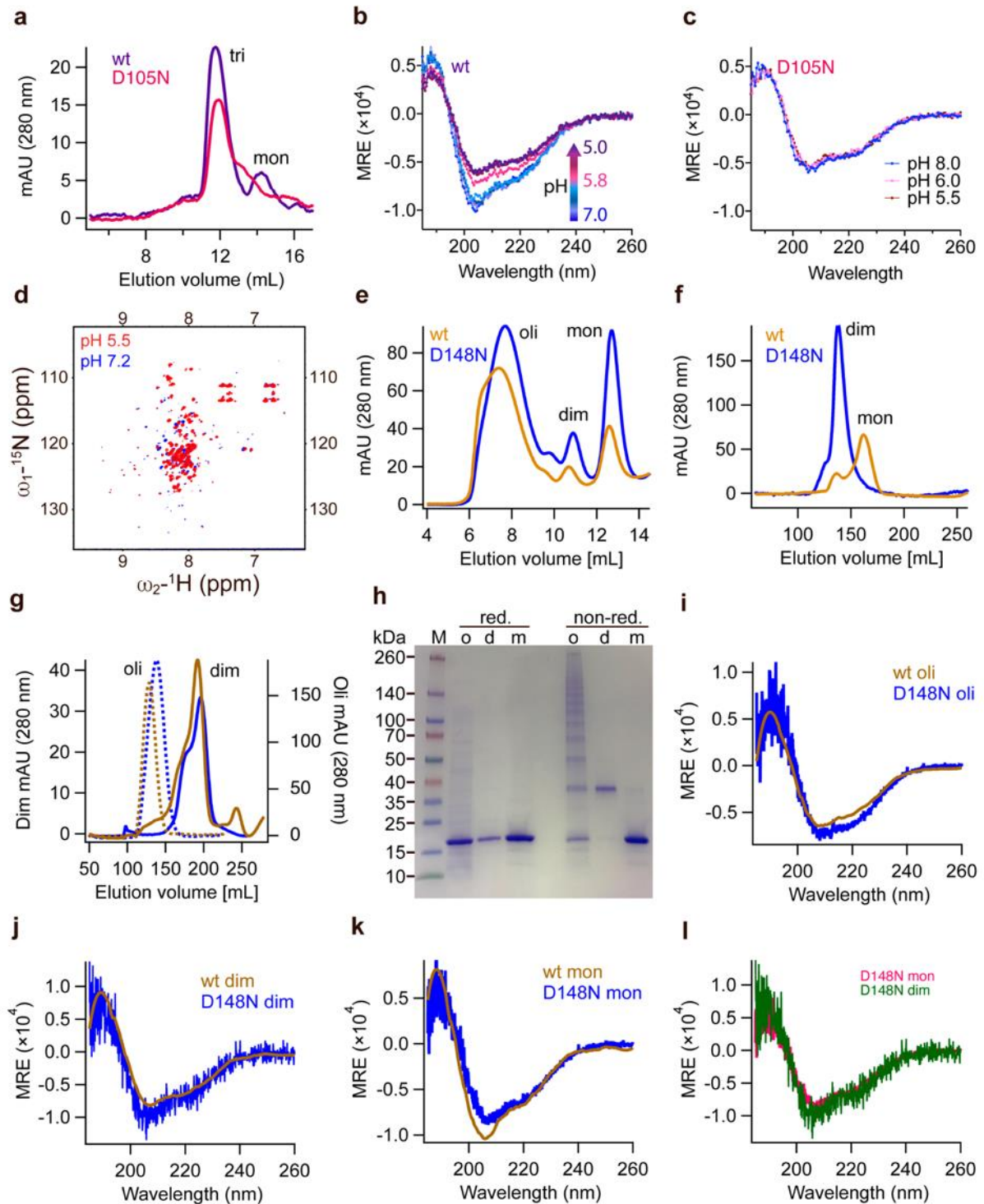
Fig. S5. Characterization of rh wildtype and Asp to Asn mutant BRICHOS. (**a**) SEC analysis of purified rh wildtype (wt) proSP-C BRICHOS (purple) and the D105N mutant (red). (**b** and **c**) CD measurements of rh wt proSP-C BRICHOS (purple) and the D105N mutant at different pHs. (**d**) NMR HSQC spectrum comparison of rh wt proSP-C BRICHOS (purple) and the D105N mutant at pH 7.2 (blue) and 5.5 (red). (**e**) SEC of rh wildtype (wt, yellow) NT*-Bri2 BRICHOS and the D148N mutant (blue) species. oli, oligomers; dim,

1220   dimers. (**f**) SEC of wildtype (wt) Bri2 BRICHOS (blue) and Bri2 BRICHOS D148N (yellow)

1221   monomer fraction prepared from corresponding fusion protein (NT*-Bri2 BRICHOS)

1222   monomers. dim, dimers; mon, monomers. (**g**) SEC of wildtype (wt) Bri2 BRICHOS (blue)

1223   and the D148N (yellow) oligomer (dash line) and dimer (solid line) fractions prepared from

1224   corresponding fusion protein (NT*-Bri2 BRICHOS) oligomer and dimer. oli, oligomers; dim,

1225   dimers. (**h**) SDS-PAGE analyses of SEC isolated rh Bri2 BRICHOS D148N species under

1226   reducing and non-reducing conditions. (**i–l**) CD spectra of rh Bri2 BRICHOS D148N

1227   monomers, dimers and oligomers and the comparison with rh wildtype (wt) Bri2 BRICHOS

1228   monomer. MRE is the mean molar residual ellipticity in $deg \cdot cm^2 \cdot dmol^{-1}$.

1229

1230

1231

1232

1233

1234

1235
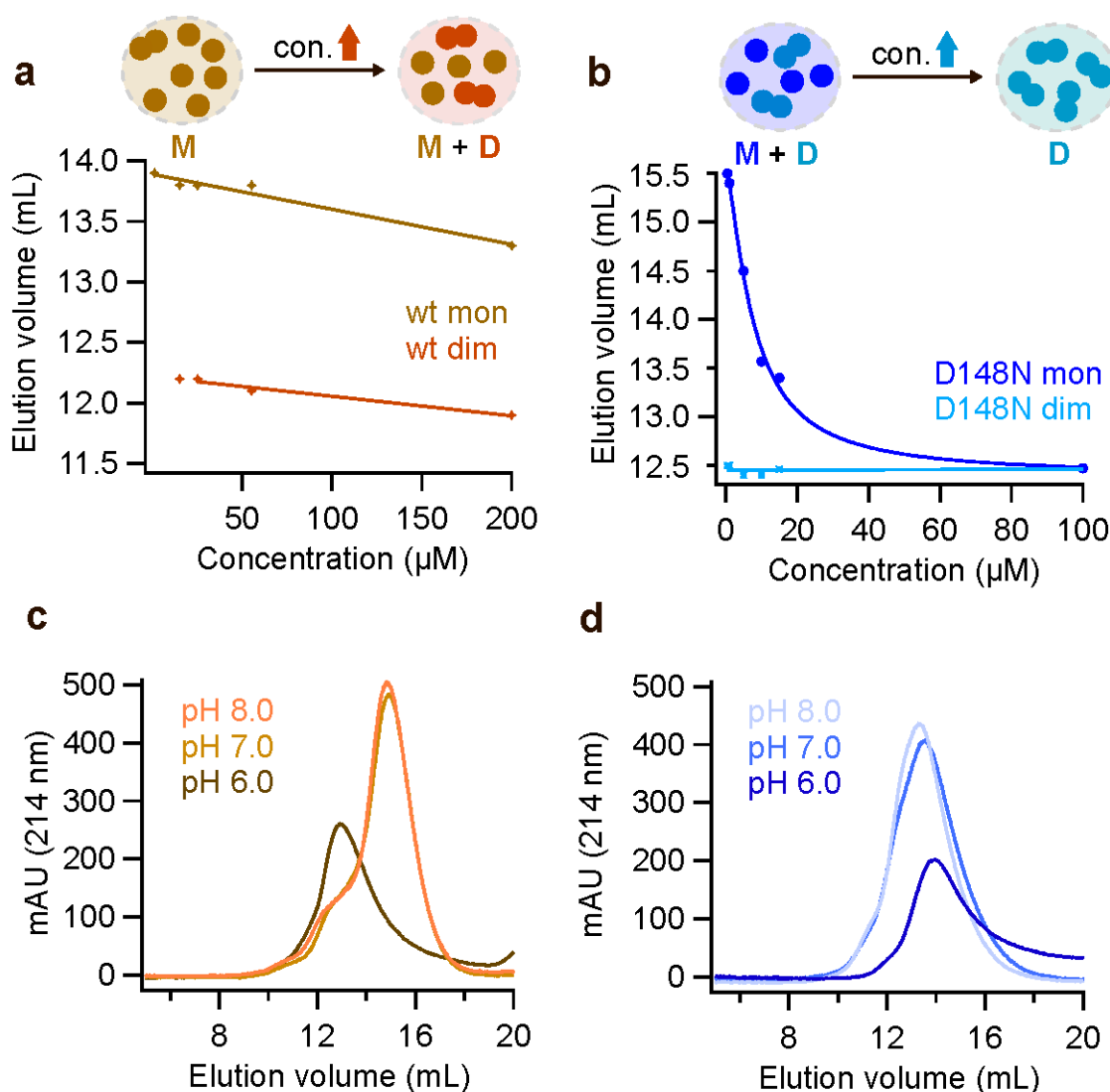
Fig. S6. Concentration and pH dependent properties of rh BRICHOS from Bri2. (**a**) Concentration-dependent dimerization of rh wildtype Bri2 BRICHOS monomers, the details are shown in **Supplementary Figure 7**. The schematic inset shows that at low concentration the rh wildtype Bri2 BRICHOS monomer fraction is purely monomeric, while with increasing concentrations dimers form. M, monomer; D, dimer. (**b**) Concentration-dependent dimerization of rh Bri2 BRICHOS D148N monomers, the details are shown in **Supplementary Figure 8**. The schematic inset shows the presence of rh Bri2 BRICHOS D148N monomers and dimers already at low concentration, while at increased concentrations all monomers form dimers. M, monomer; D, dimer. pH dependent dimerization of (**c**) 10 µmol L^{-1} rh wildtype Bri2 BRICHOS monomers and (**d**) rh Bri2 BRICHOS D148N monomers analysed by SEC.

50
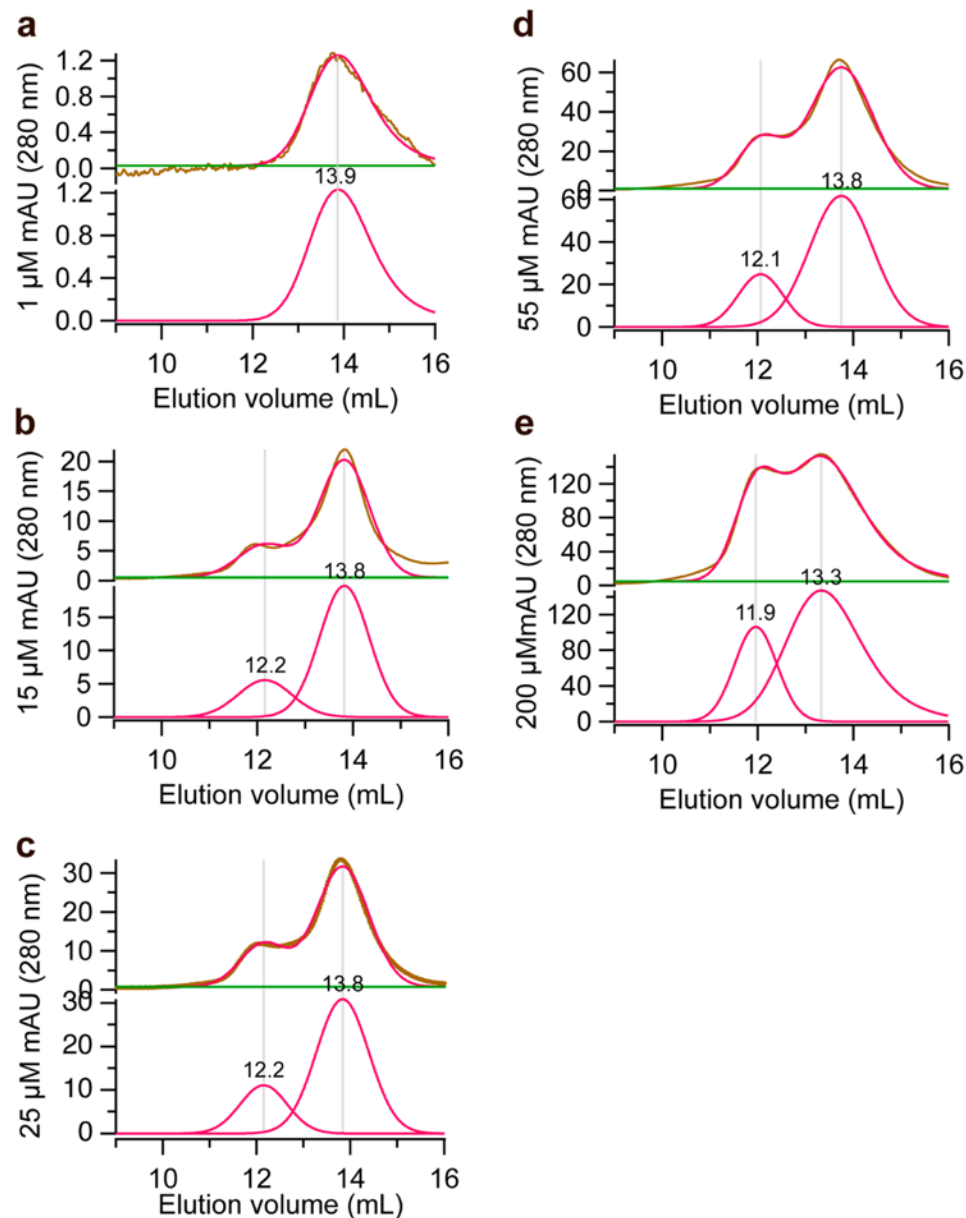
Fig. S7. Rh wildtype Bri2 BRICHOS monomer concentration-dependent dimerization. SEC analysis of rh wildtype Bri2 BRICHOS monomer at concentrations of 1 (**a**), 15 (**b**), 25 (**c**), 55 (**d**) and 200 μmol L^{-1} (**e**). The top panel of each sub-figure is the raw SEC data (yellow) with gaussian fitted (red). The lower panel of each sub-figure is the multiple gaussian peak fitting (red) and the number on the top of each peak represents the elution volume.
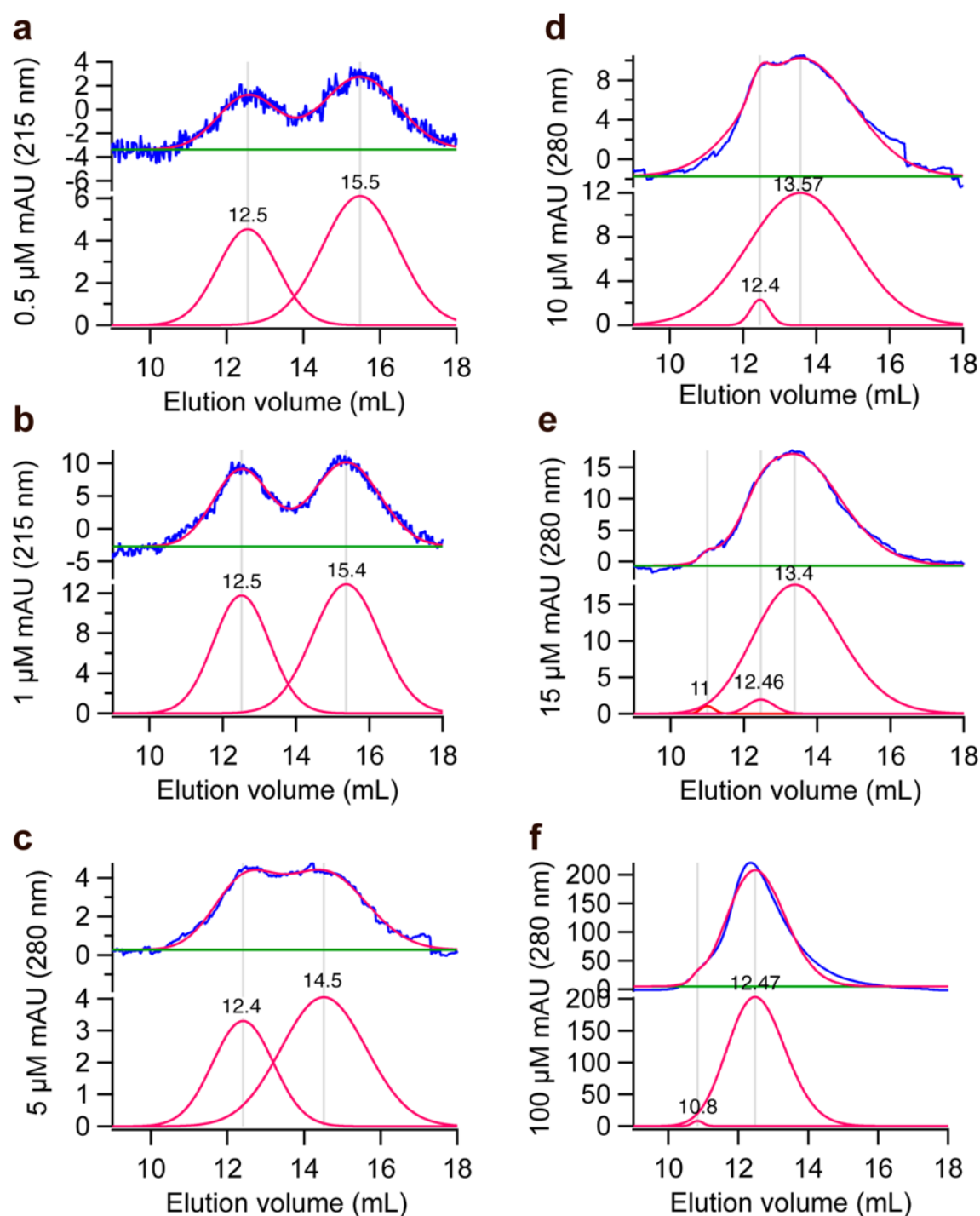
Fig. S8. Rh Bri2 BRICHOS D148N monomer concentration-dependent dimerization. SEC analysis of rh Bri2 BRICHOS D148N monomer at concentrations of 0.5 (**a**), 1 (**b**), 5 (**c**), 10 (**d**), 15(**e**) and 100 µmol L^{-1} (**f**). The top panel of each sub-figure is the unprocessed data (yellow) with gaussian fitted (red). The lower panel of each sub-figure is the gaussian peak fitting (red) and the number on the top of each is the relevant elution volume.
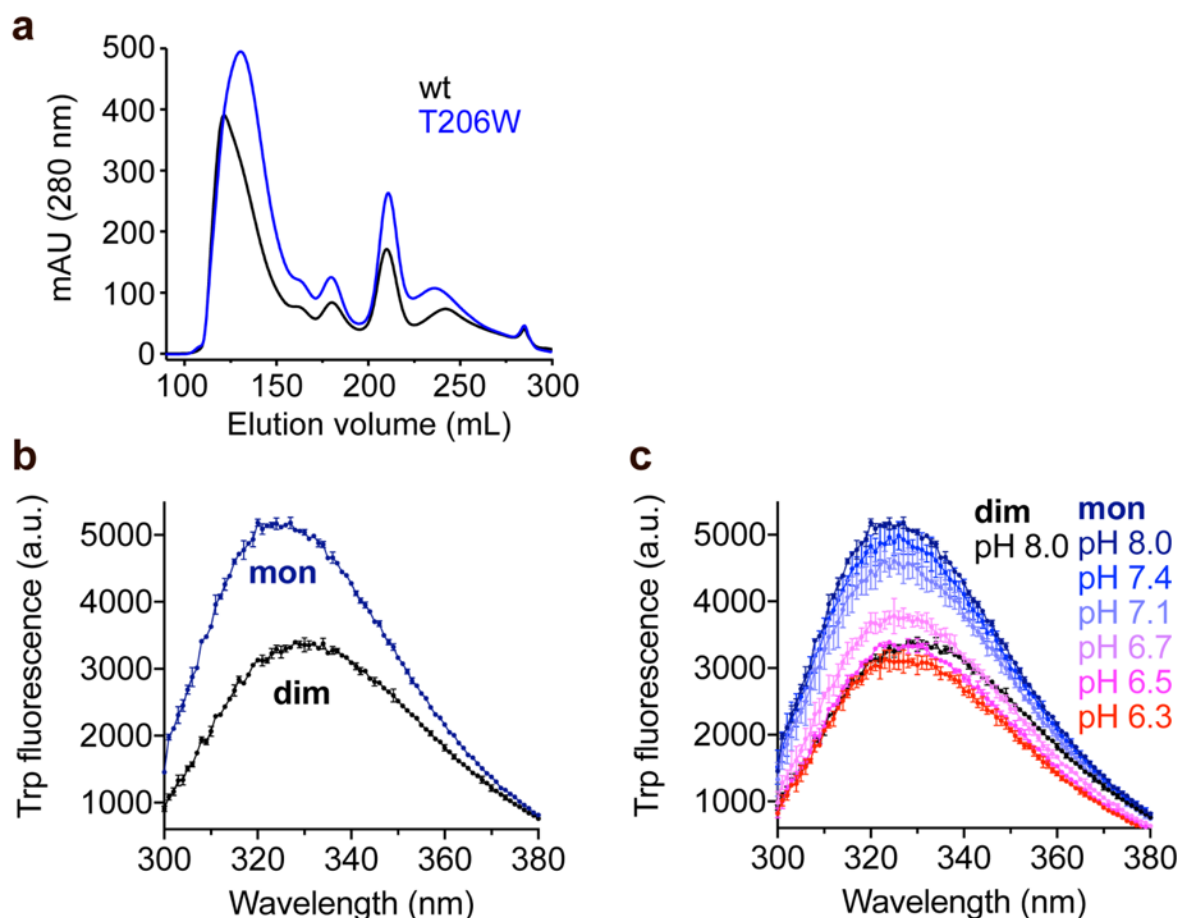
52

1264

1265

1266

Fig. S9. Trp fluorescence of rh Bri2 BRICHOS T206W mutant. (**a**) SEC of rh wildtype NT*-Bri2 BRICHOS and the rh NT*-Bri2 BRICHOS T206W mutant. (**b**) Rh Bri2 BRICHOS T206W monomers and dimers were diluted to 2 μmol L^{-1} in 20 mmol L^{-1} NaPi, 0.2 mmol L^{-1} EDTA at pH 8.0. (**b**) Rh Bri2 BRICHOS T206W monomers at different pHs from pH 6.3 to pH 8.0 were subjected to Trp fluorescence measurements, while the dimers were measured at pH 8.0. All the samples were prepared in duplicates, and excited at 280 nm (5 μm bandwidth) and fluorescence emission from 300–400 nm (10 μm bandwidth,1 nm step interval) was recorded. For the final fluorescence intensities, the results were corrected by subtracting the background fluorescence. The data are presented as means ± standard deviations.
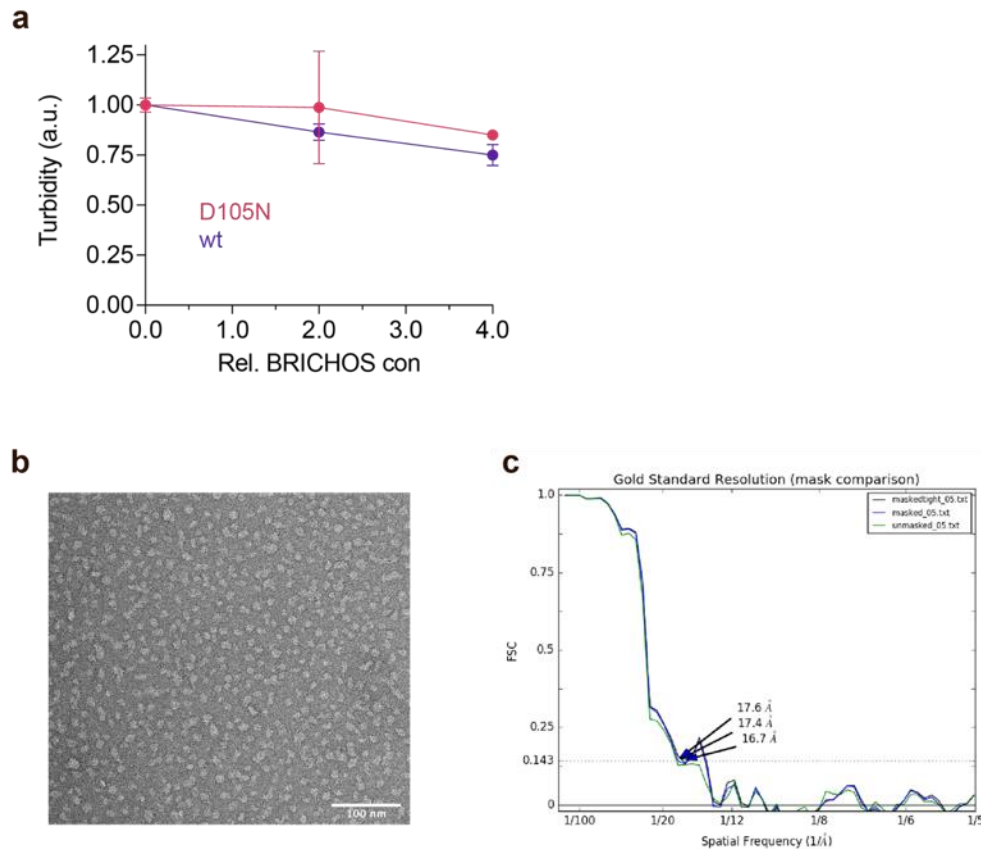
Fig. S10. Electron microscopy analyses of rh Bri2 BRICHOS D148N oligomers. (**a**) Effects of rh proSP-C BRICHOS variants on CS aggregation at different molar ratios of BRICHOS:CS. The data are presented as means ± standard deviations. (**b**) Raw TEM micrograph of negatively stained rh Bri2 BRICHOS D148N oligomers. (**c**) The Fourier shell correlation (FSC) indicates a resolution of ~17 Å for the reconstructed 3D density map determined at an FSC-value of 0.143 (dotted lines).
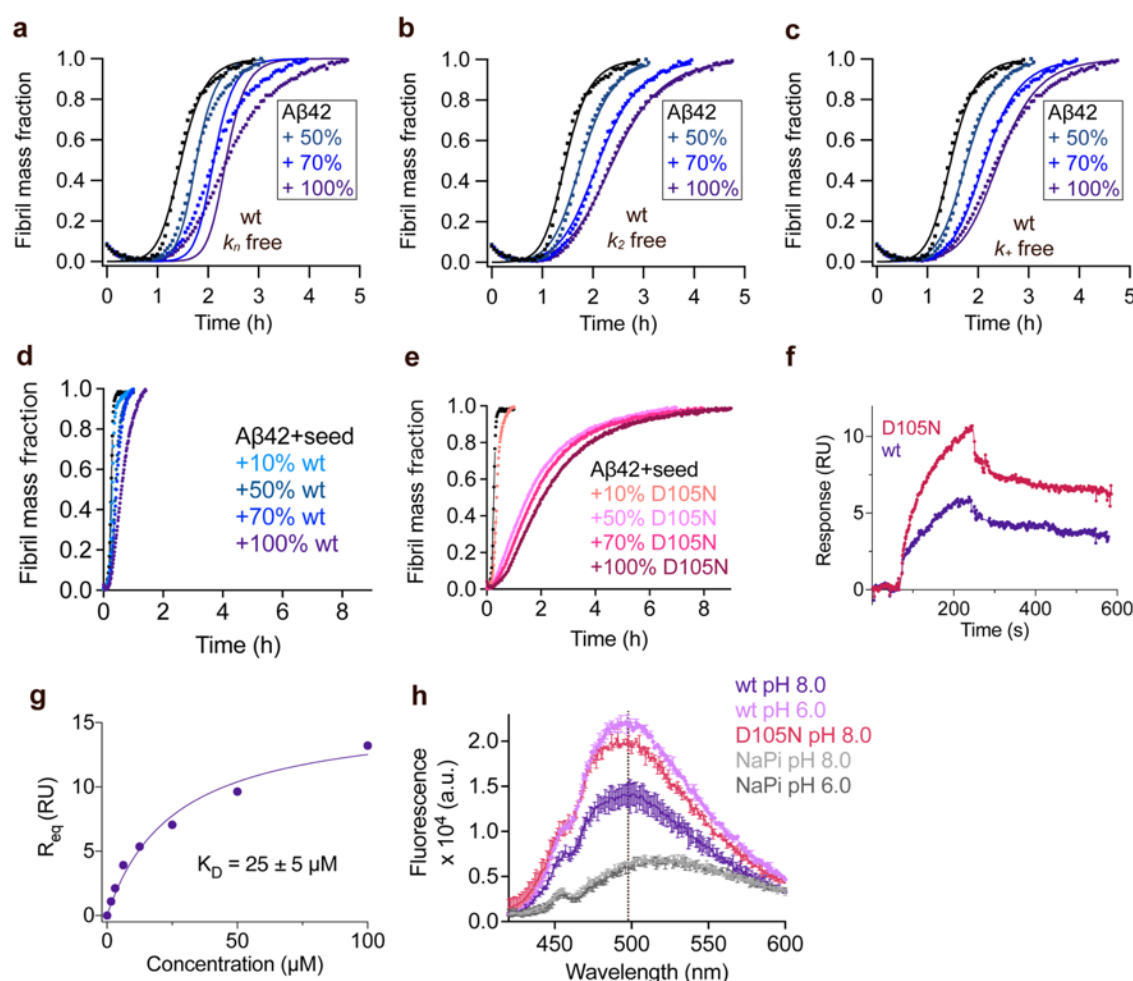
Fig. S11. Rh wildtype proSP-C BRICHOS interferes with Aβ42 fibril formation. (**a–c**) Aggregation kinetics of 3 μmol L^{-1} Aβ42 in the presence of rh wildtype (wt) proSP-C BRICHOS at concentrations: 0 (black), 50 (cyan), 70 (blue), or 100% (purple) molar percentage referred to monomeric subunits relative to Aβ42 monomer concentration. The global fits (solid lines) of the aggregation traces (cross) were constrained such that only one single rate constant is the free fitting parameter. (**d** and **e**) Seeded aggregation traces of 3 μmol L^{-1} Aβ42 with 0.6 μmol L^{-1} preformed Aβ42 fibril seeds in the presence of different concentration of rh wildtype proSP-C BRICHOS (**d**) and the D105N mutant (**e**). (**f**) Analysis of rh wildtype (wt) proSP-C BRICHOS (purple) and the D105N mutant (red) binding to Aβ42 monomers detected by SPR. 25 μmol L^{-1} rh wildtype proSP-C BRICHOS and the D105N mutant were injected in over the chip surfaces, respectively. The response from the blank surface was subtracted from the immobilized surface response. (**g**) Steady state affinity for rh proSP-C BRICHOS D105N to immobilised Aβ42 monomers. Different concentrations of rh proSP-C BRICHOS D105N mutant, *i.e.* 0, 1.56, 3.13, 6.25, 12.5, 25, 50 and 100 μmol L^{-1}, were individually injected over the chip surfaces. Steady state affinity was estimated by

1301   plotting the maximum binding responses versus BRICHOS concentrations. (**h**) Fluorescence

1302   emission of 2 μmol L^{-1} bis-ASN in sodium phosphate buffer at pH 8.0 (gray) or 6.0 (black) or

1303   in the presence of 1 μmol L^{-1} rh wildtype proSP-C BRICHOS at pH 8.0 or 6.0 and the

1304   D105N mutant.

1305

1306

1307

1308

1309

1310

1311

1312
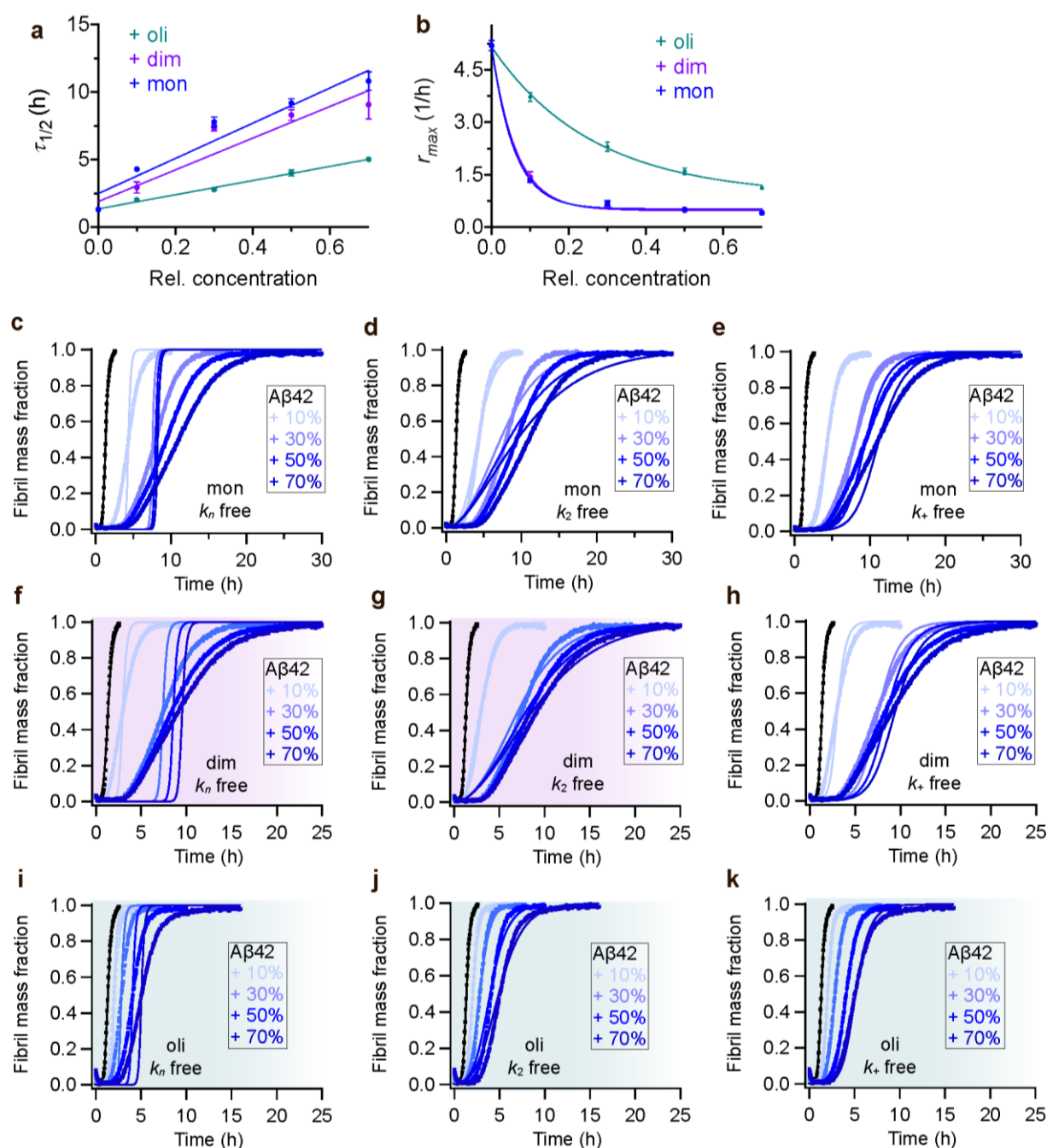
1313

1314   **Fig. S12. Rh Bri2 BRICHOS D148N inhibition of Aβ42 fibril formation.** Values for $\tau_{1/2}$

1315   (**a**) and r_{max} (**b**) extracted from the sigmoidal fitting of Aβ42 aggregation traces in the

1316   presence of different concentrations of rh Bri2 BRICHOS D148N species as shown in (**c–k**).

1317   (**c–e**) Aggregation kinetics of 3 μmol L^{-1} Aβ42 in the presence of rh Bri2 BRICHOS D148N

1318   monomers at different concentrations. The global fits (solid lines) of the aggregation traces

1319   (cross) were constrained such that only one single rate constant is the free fitting parameter,

1320   indicated in each panel. χ^2 values describing the quality of the fits: 62 for k_n free, 11.2 for k_2

1321   free and 3.7 for k_+ free. (**f–h**) Aggregation kinetics of 3 μmol L^{-1} Aβ42 in the presence of rh

1322   Bri2 BRICHOS D148N dimers at different concentrations. The global fits (solid lines) of the

1323 aggregation traces (cross) were constrained such that only one single rate constant is the free

1324 fitting parameter, indicated in each panel. χ^2 values describing the quality of the fits: 43 for

1325 k_n free, 3.9 for k_2 free and 7.8 for k_+ free. (**i–k**) Aggregation kinetics of 3 μmol L^{-1} Aβ42 in

1326 the presence of rh Bri2 BRICHOS D148N oligomers at different concentrations. The global

1327 fits (solid lines) of the aggregation traces (cross) were constrained such that only one single

1328 rate constant is the free fitting parameter. χ^2 values describing the quality of the fits: 8.6 for

1329 k_n free, 1.4 for k_2 free and 0.4 for k_+ free. For the different D148N species, both k_2 and k_+ as

1330 sole free fitting rate, the fibrillization traces were described with similar χ^2 values,

1331 suggesting both k_2 and k_+ might be affected, like the wildtype species.

1332

1333

1334

1335 **Supplementary Table.**

1336 **Table S1. Species distribution and pairwise alignment of the multiple BRICHOS**
1337 **domains.** See separate file.

1338 **Table S2. Summary of statistics performed in Fig. 3b and d.**

1339

1340 **Source data:**

1341 **Figure 3-source data.**

1342 **Figure 4-source data.**

1343 **Figure 5-figure supplement 5-source data**

1344

1345